THE ASTROPHYSICAL JOURNAL, 508:106–122, 1998 November 20

THE *COBE* DIFFUSE INFRARED BACKGROUND EXPERIMENT SEARCH FOR THE COSMIC INFRARED BACKGROUND. IV. COSMOLOGICAL IMPLICATIONS

E. DWEK,[1] R. G. ARENDT,[2] M. G. HAUSER,[3] D. FIXSEN,[2] T. KELSALL,[1] D. LEISAWITZ,[4] Y. C. PEI,[3] E. L. WRIGHT,[5] J. C. MATHER,[1] S. H. MOSELEY,[1] N. ODEGARD,[2] R. SHAFER,[1] R. F. SILVERBERG,[1] AND J. L. WEILAND[2]

Received 1998 January 7; accepted 1998 June 22

ABSTRACT

A direct measurement of the extragalactic background light (EBL) can provide important constraints on the integrated cosmological history of star formation, metal and dust production, and the conversion of starlight into infrared emission by dust. In this paper we examine the cosmological implications of the recent detection of the EBL in the 125 to 5000 μm wavelength region by the Diffuse Infrared Background Experiment (DIRBE) and Far Infrared Absolute Spectrophotometer (FIRAS) on board the *Cosmic Background Explorer* (*COBE*). We first show that the 140 and 240 μm isotropic residual emission found in the DIRBE data cannot be produced by foreground emission sources in the solar system or the Galaxy. The DIRBE 140 and 240 μm isotropic residuals, and by inference the FIRAS residuals as well, are therefore extragalactic. Assuming that most of the 140 and 240 μm emission is from dust yields a 2 σ lower limit of $\nu I(\nu) \approx 5$ nW m^{-2} sr^{-1} for the EBL at 100 μm. The integrated EBL detected by the *COBE* between 140 and 5000 μm is $\sim$16 nW m^{-2} sr^{-1}, roughly 20%–50% of the integrated EBL intensity expected from energy release by nucleosynthesis throughout cosmic history. This also implies that at least $\sim$5%–15% of the baryonic mass density implied by big bang nucleosynthesis has been processed through stars. The *COBE* observations provide important constraints on the cosmic star formation rate, and we calculate the EBL spectrum for various star formation histories. The results show that the UV and optically determined cosmic star formation rates fall short in producing the observed 140 to 5000 μm background. The *COBE* observations require the star formation rate at redshifts of $z \approx 1.5$ to be larger than that inferred from UV-optical observations by at least a factor of 2. This excess stellar energy must be mainly generated by massive stars, since it otherwise would result in a local *K*-band luminosity density that is larger than observed. The energy sources could either be yet undetected dust-enshrouded galaxies, or extremely dusty star-forming regions in observed galaxies, and they may be responsible for the observed iron enrichment in the intracluster medium. The exact star formation history or scenarios required to produce the EBL at far-IR wavelengths cannot be unambiguously resolved by the *COBE* observations and must await future observations.

Subject headings: cosmology: observations — diffuse radiation — dust, extinction — galaxies: evolution — infrared: general

1. INTRODUCTION

The extragalactic background light (EBL) consists of the cumulative emission from various pregalactic objects, protogalaxies, and galaxies throughout the evolution of the universe. Its detection is a subject of great scientific interest and the main purpose of the Diffuse Infrared Background Experiment (DIRBE) on the *Cosmic Background Explorer* (*COBE*) spacecraft (Boggess et al. 1992). The DIRBE was designed to search for a cosmic infrared (IR) background, which is presumed to be spatially isotropic. The detection of the EBL at IR wavelengths is greatly hampered by the presence of strong foreground emission. The removal of these various layers of emission without affecting any potential extragalactic component is a formidable task that has been described by the DIRBE team in three previous papers in this series: Hauser et al. (1998, hereafter Paper I) summarized limits and detections of the EBL, Kelsall et al. (1998, Paper II) described the subtraction of the interplanetary dust scattering and emission component, and Arendt et al. (1998, Paper III) described the subtraction of the Galactic stellar and diffuse interstellar emission components. A residual may be considered as extragalactic in origin if its signal is positive and isotropic. Hauser et al. (1998) described in detail the tests conducted to examine whether significant residual emission exists at each of the DIRBE wavelengths and, if so, whether that emission is isotropic. These studies resulted in upper limits on the EBL in the 1.25–100 μm region, and in the detection of a positive isotropic signal at 140 and 240 μm. Furthermore, a detailed analysis of the data obtained with the Far Infrared Absolute Spectrophotometer (FIRAS) instrument on the *COBE* resulted in a detection of the EBL in the 125–5000 μm region (Fixsen et al. 1998, Paper V). The DIRBE and FIRAS isotropic residuals can be summarized as

$$\begin{aligned} \nu I_\nu &= 25.0 \pm 6.9 \text{ nW m}^{-2} \text{ sr}^{-1} \quad \text{at } 140\ \mu\text{m} \quad \text{(Paper I)} \\ &= 13.6 \pm 2.5 \text{ nW m}^{-2} \text{ sr}^{-1} \quad \text{at } 240\ \mu\text{m} \quad \text{(Paper I)} \\ &= A\lambda_{100}^{-\alpha}\, \nu B_\nu(T_d) \quad \text{at } 125\text{–}5000\ \mu\text{m} \quad \text{(Paper V)}, \end{aligned} \tag{1}$$

[1] Laboratory for Astronomy and Solar Physics, Code 685, NASA/Goddard Space Flight Center, Greenbelt, MD 20771; eli.dwek@gsfc.nasa.gov.
[2] Raytheon STX, Code 685, NASA/GSFC, Greenbelt, MD 20771.
[3] Space Telescope Science Institute, 3700 San Martin Drive, Baltimore, MD 21218.
[4] Laboratory for Astronomy and Solar Physics, Code 681, NASA/Goddard Space Flight Center, Greenbelt, MD 20771.
[5] University of California at Los Angeles, Astronomy Department, Los Angeles, CA 90024-1562.

where B_ν is the Planck function, $T_d = 18.5 \pm 1.2$ K, $\alpha = 0.64 \pm 0.12$, $A = (1.3 \pm 0.4) \times 10^{-5}$, and λ_{100} is the wavelength in units of 100 μm. The DIRBE detections are smaller than, but consistent with, the detections reported by Schlegel, Finkbeiner, & Davis (1998). The FIRAS detections of Fixsen et al. (1998) are consistent with those of the DIRBE, and, at wavelengths longer than 300 μm, generally similar to the tentative detections reported by Puget et al. (1996). A more detailed discussion of the comparison is given by Hauser et al. (1998) and Fixsen et al. (1998). The integrated intensity of the background detected in the DIRBE 140 and 240 μm bands is 10.3 nW m^{-2} sr^{-1} and that detected by the FIRAS in the 240 to 5000 μm region is 5.3 nW m^{-2} sr^{-1}, giving a total EBL intensity of $\sim$16 nW m^{-2} sr^{-1} in the $\sim$125 to 5000 μm wavelength interval.

The purpose of this paper is to discuss some of the implications of these *COBE* measurements. We show in § 2 and the Appendix that local sources in the solar system or the Galaxy cannot provide significant contributions to the residual isotropic emission at 140 and 240 μm. No known component of the solar system can produce an isotropic emission component at the observed intensity in these two DIRBE bands. Furthermore, a hypothetical solar system component consistent with the various constraints provided by the DIRBE observations is unlikely to survive or be maintained over the lifetime of the solar system. Likewise, we argue that no Galactic dust component can produce the observed far-IR isotropic emission component. The residual emission detected by the DIRBE and FIRAS instruments is therefore of extragalactic origin. Adopting the extragalactic nature of the 140 and 240 μm residuals, we show that the detections in these bands imply a lower limit on the extragalactic contribution at 100 μm as well (§ 3).

Various cosmological implications of the *COBE* detections are addressed in this paper.

1. *The origin of the EBL.*—Two major energy sources can contribute to the observed EBL: nuclear and gravitational. The nuclear contribution consists of the energy released in stellar nucleosynthetic processes. This energy is radiated predominantly at UV-visual wavelengths and either redshifted or absorbed and reradiated by dust into the infrared ($\lambda \gtrsim 1$ μm) wavelength region. Gravitational potential energy dominates the energy released by brown dwarfs, accreting black holes, and gravitationally collapsing systems and may make a significant contribution to the EBL (see Bond, Carr, & Hogan 1986, 1991, hereafter BCH86, BCH91; Carr 1992, and references therein). Black holes in active galactic nuclei (AGNs) may contribute a significant fraction of the EBL in the mid-IR ($\approx$10–50 μm) wavelength region (Granato, Franceschini, & Danese 1996), and AGNs may be contributing to the IR energy released in starbursts as well. However, the magnitude of the AGN contribution to the diffuse IR background is highly uncertain, since it depends on the amount of dust and the geometry of the torus around the active nucleus. A third possible source of energy is that released by decaying relic particles (BCH86, BCH91). Since the infrared EBL should contain a significant fraction of *all* the energy released in the universe since the recombination epoch, its measurement can constrain the relative contribution of the various energy sources. For example, as discussed in Paper I (see also Fig. 9 in this paper), the intensity predicted for some nonnuclear energy sources (e.g., BCH86, BCH91) falls above the DIRBE upper limits, indicating that these models are not viable without significant modifications.

2. *The evolution of galaxies.*—The intensity and spectrum of the EBL contains information on the evolution of the number density, luminosity, and spectral energy distribution (SED) of galaxies over the history of the universe. The number density of galaxies is expected to evolve as galaxies merge and undergo a starbursting activity or fade out of view. Deep galaxy counts using data obtained by the *Infrared Astronomical Satellite* (*IRAS*) suggest either mild luminosity evolution or comoving density evolution with redshift up to $\lesssim 0.01$ (Ashby et al. 1996). On theoretical grounds, the galaxy luminosity and SED are functions of its star formation activity, metallicity, and dust content, all evolving quantities that determine its far-IR appearance (e.g., Dwek & Városi 1996; Dwek 1998). The *COBE* data can therefore be used to set constraints on these evolutionary processes.

3. *The star formation history of the universe.*—The spectrally integrated EBL at IR wavelengths should contain much of the energy associated with the production of elements throughout the history of the universe. The EBL spectrum depends on the details of the cosmic star formation history and the transport of the stellar energy through the ambient dusty environment. *Hubble Space Telescope* (*HST*) observations of the Hubble deep field (HDF) provided important new constraints on the star formation rate (SFR) at redshifts between $\sim$2 and 5 (Madau et al. 1996). These observations suggest that the cosmic SFR at these redshifts falls significantly below those in the more local universe (Lilly et al. 1996), suggesting that the cosmic star formation activity peaked at redshifts of about 1–1.5. However, an important ongoing debate is whether the UV and optically (UVO) derived SFR inferred from ground-based and *HST* observations severely underestimates the actual star formation rate in the universe. Using *Infrared Space Observatory* (*ISO*) observations of the HDF, Rowan-Robinson et al. (1997, hereafter RR97) argued that the *HST* missed a significant fraction of the star formation activity that takes place in dust-enshrouded galaxies at $z \gtrsim 2$. The *COBE* data provide an important constraint on the star formation history of the universe and can therefore confirm (or rule out) the presence of dust-enshrouded galaxies or star-forming regions that may have led to an underestimate of the cosmic SFR.

To address the origin of the EBL, we examine whether the intensity detected by the DIRBE and FIRAS is consistent with that expected from the He-enrichment and metal formation in the universe. Assuming a nuclear origin for the observed EBL and a cosmic star formation history, one can set a lower limit on the mass fraction of baryonic matter that must have been processed into He and heavier elements in stars (§ 4). To examine whether the *COBE* observations suggest any galaxy evolution, we develop a simple model to calculate the intensity and spectrum of the EBL (§ 5). Using a population synthesis model, we calculate the spectral luminosity density produced by unattenuated starlight at each redshift. Then, for a given magnitude of visual extinction and a Galactic extinction law, we calculate the fraction of starlight that is absorbed by dust and converted into IR emission at each redshift. For simplicity, we assume

that the extinction is constant as a function of redshift, and that the emitted IR spectrum is identical in shape to that produced by *IRAS* galaxies in the local universe. The spectrum of the EBL is then obtained by integrating the comoving spectral luminosity density of the attenuated starlight and the emitting dust over redshift. By examining the extent to which the spectrum calculated by this simple model deviates from the observed EBL, we can obtain clues to possible galactic evolutionary processes. To examine the constraints provided by the *COBE* on the cosmic star formation history, we calculate the EBL spectrum for various star formation histories. The resulting EBL spectra (as well as those derived by other authors) are compared to the observational constraints in § 6. The results of the paper are briefly summarized in § 7. A value of $H_0 = 50$ km s^{-1} Mpc^{-1} for the Hubble constant, and a flat universe ($\Omega_0 = 1$), with a zero cosmological constant ($\Omega_\Lambda = 0$) is adopted throughout this paper.

2. POSSIBLE ISOTROPIC LOCAL CONTRIBUTIONS TO THE 140 AND 240 μm RESIDUAL EMISSION

Before studying the cosmological implications of the DIRBE results, we must examine whether local sources in the solar system or in the Galaxy can contribute a significant fraction of the observed residual emission. Given a ν^n emissivity law, the temperature of a radiating particle is determined by the emissivity index n and by the 140 and 240 μm intensities attributed to these sources. Further constraints on the temperature of the source are placed by the DIRBE 1.25–100 μm upper limits (Paper I), and the FIRAS dark sky limits of ~ 12.2 and 1.3 nW m^{-2} sr^{-1} at 340 and 650 μm, respectively (Shafer et al. 1998).

Figure 1 depicts the spectra of various hypothetical thermal sources that can contribute to the 140 and 240 μm residual emission, for blackbody emitters characterized by an $n = 0$ emissivity law (Fig. 1*a*), and for dust particles characterized by an $n = 2$ emissivity law (Fig. 1*b*). The highest temperatures consistent with the DIRBE upper limits are 100 K for blackbody particles and 40 K for $n = 2$ dust particles. Blackbodies with temperatures lower than 18 K will violate the FIRAS dark sky limits. This temperature is slightly above the value of ~ 16 K attained by such particles if they are only heated by the local interstellar radiation field (ISRF). The first firm conclusion that we can draw from these figures is that neither stars, stellar remnants, nor brown dwarfs can possibly contribute to the emission at these wavelengths at the level required to account for a significant fraction of the residual emission. To further characterize the properties of the potential foreground emission sources, we need to specify their physical location, i.e., whether they reside in the interstellar medium (ISM) or in the solar system.

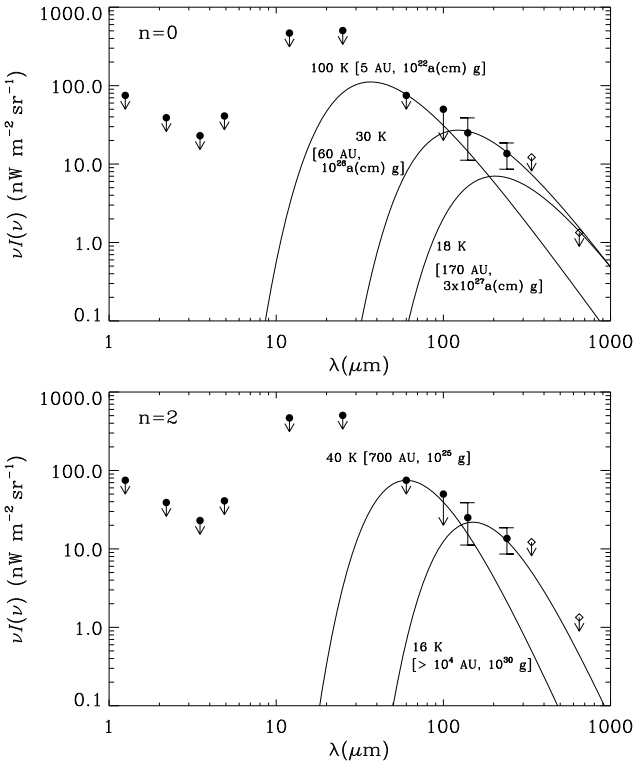

FIG. 1.—Spectra of hypothetical clouds of particles that can contribute significantly to the residual emission at 140 and 240 μm within the *COBE* observational constraints. Filled circles represent the DIRBE upper limits and detections (Paper I), and the open diamonds represent the FIRAS dark sky limits (Shafer et al. 1998). Cloud particles radiate with a ν^n emissivity law. *Top:* Constraints for $n = 0$ particles. Particle temperatures are constrained to be below 100 K by the DIRBE upper limits at wavelengths ≤ 100 μm and above 18 K by the FIRAS dark sky limits. Particles with a temperature of 30 K can, in principle, produce *all* the 140 and 240 μm residual emission in these bands. Also shown in square brackets are the heliocentric distances and masses calculated for such clouds, if they were located in the solar system. *Bottom:* Constraints for $n = 2$ particles. The lower temperature limit is determined by the interstellar radiation field.

2.1. *A Solar System Isotropic Emission Component*

2.1.1. *The Required Characteristics of a Radiating Cloud of Solar System Dust Particles*

To give rise to an isotropic emission component, any emitting sources within the solar system must have a spherically symmetric distribution, either centered on the Earth or centered on the Sun and located at a sufficiently large distance to appear isotropic when viewed from the Earth. The measured DIRBE intensities were independent of zenith distance, ruling out an Earth-centered cloud of particles. Any local emission component must therefore be Sun-centered, a conclusion supported by the limits on the source temperature and distance discussed below. We will also assume that such a cloud was assembled during, or shortly after, the formation of the solar system (about $\tau_\odot = 4.5$ billion yr ago), since it is unlikely that collisions could have produced a spherical distribution of particles after most of the solar system material settled into a disk.

Given an emissivity law and the particle temperature T, the cloud's distance from the Sun d can be calculated from the energy balance equation:

$$\pi a^2(1 - A)\left(\frac{L_\odot}{4\pi d^2} + \frac{c}{4\pi} U_{\rm ISRF}\right) = 4\pi a^2 \sigma T^4 C(T) , \quad (2)$$

where a is the radius of the emitting particles, A their effective albedo, $C(T)$ is the Planck-averaged value of their emissivity, and $U_{\rm ISRF}$ is the energy density of the local ISRF. Assuming an albedo of 0.5, large particles will attain temperatures of about 235 K at a distance of 1 AU from the Sun, whereas particles with optical properties similar to interstellar dust particles (Draine & Lee 1984) will have typical temperatures of ~ 350 K. The distance d at which a

particle attains a temperature T can then be written as

$$d(\mathrm{AU}) = \left(\frac{T}{235}\right)^{-2} \quad \text{for blackbody particles } (n = 0)\,,$$
$$= \left(\frac{T}{350}\right)^{-3}\left[1 - \left(\frac{16}{T}\right)^{6}\right]^{-1/2} \qquad (3)$$

for dust particles particles ($n = 2$).

At any distance from the Sun, the particles will always be heated by the ISRF. This heating source is less important for blackbodies, but gives dust particles a minimum temperature of about 16 K. Given the heliocentric distance of the cloud, its 140 or 240 μm brightness is given by

$$M_c = \frac{4\pi d^2 I(\lambda)}{\kappa(\lambda) B_\lambda(T)}\,, \qquad (4)$$

where $\kappa(\lambda)$ is the mass absorption coefficient of the particles at wavelength λ. For blackbodies, κ is wavelength independent and given by $3/(4\rho a)$, where $\rho \approx 1$–3 g cm^{-3} is the mass density of the radiating particle. Small dust particles will be characterized by a ν^2 emissivity law and a value of $\kappa = 7.2$ cm^2 g^{-1} at $\lambda = 240$ μm (Draine & Lee 1984).

The resulting cloud heliocentric distances (in astronomical units) and masses are indicated in square brackets in Figures 1*a* and 1*b*. For blackbodies, the masses were calculated for particles with 1 cm radius. Cloud masses scale linearly with particle radius and also depend on the particle albedo and mass density. For $n = 2$ dust particles, cloud masses only depend on the mass absorption coefficient and albedo. The figures show that cloud distances range from $\sim$5 to 170 AU for $n = 0$ ($\gtrsim$700 AU for $n = 2$) and cloud masses range from $\sim 10^{22} a$(cm) to $10^{27} a$(cm) g for $n = 0$ ($\sim 10^{25}$ to 10^{30} g for $n = 2$). Depending on their origin, cloud particles could have a higher albedo and a lower mass density than assumed, as has been suggested for Kuiper Belt particles (Teplitz et al. 1998). At a fixed temperature, namely that required to produce the observed DIRBE detections (see Fig. 1), a lower albedo of $A \sim 0.05$ will place the dust cloud at a larger distance, *increasing* the cloud mass by about a factor of 2 above that given in the figure. On the other hand, a significantly lower mass density of $\sim$0.5–1 g cm^{-3}, characteristic of icy particles, will *decrease* the cloud mass by a factor of $\sim$3–6. These numbers should serve as a guide for the uncertainties in the estimated cloud masses. For comparison, distances and masses of selected *known* solar system components are given in Table 1 (Leinert 1996). The limits on the source temperature and distance provide an additional argument that rules out the possibility that a significant part of the DIRBE residual emission originates from any ($T \sim 300$ K) Earth-centered distribution of particles.

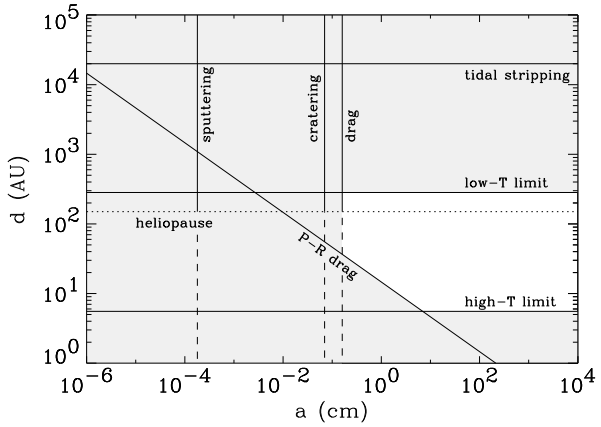

FIG. 2.—Size-distance [a(cm), d(AU)] parameter space that must be occupied by any interplanetary cloud of particles that produces a significant isotropic signal in the DIRBE 140 and 240 μm bands. Shaded regions indicate regions in (a, d) parameter space that are not stable over the lifetime of the solar system or are excluded by the temperature constraints imposed by the DIRBE data. The timescales for the various destructive processes are summarized in § 2 and the Appendix.

Any cloud of particles in the solar system will be subject to various forces and disruptive processes: radiation pressure and solar gravity; thermal and kinetic sputtering, grain-grain collisions, and collisional drag as the solar system moves through the interstellar medium; and gravitational perturbations from passing stars. Each one of these processes will tend to erode or disrupt the cloud of particles. In the Appendix we examine the lifetime of the cloud against the various interactions with the Sun, the ISM, and passing stars.

2.1.2. *The Stability of a Cloud of Solar System Dust Particles*

Figure 2 shows the [a(cm), d(AU)] parameter space that must be occupied by any interplanetary material that could significantly contribute to the DIRBE residual 140 and 240 μm emission. Shaded areas represent regions that are either excluded by the temperature limits of the cloud or where the material would be eroded due to the various effects considered in the Appendix on timescales shorter than the lifetime of the solar system. The horizontal lines marked "high-T limit" and "low-T limit" indicate the heliocentric distances below and above which the particle temperatures fall beyond the values allowed in Figure 1*a* (particles with an $n = 0$ emissivity law). Both limits are shifted to larger

TABLE 1

INTENSITY OF INTERPLANETARY COMPONENTS

Component	Distance (AU)	Temperature (K)	Mass (g)	νI_ν(240 μm) (nW m^{-2} sr^{-1})	Isotropy
Oort cloud	2×10^4 to 10^5	5	4×10^{28}	8×10^{-6}	Yes
Inner Oort cloud	10^3 to 2×10^4	10	2×10^{29}	1×10^{-3}	Yes
Kuiper Belt	40–100	40	$<6 \times 10^{27}$	0.02	No
Kuiper Belt dust	40–100	40	6×10^{27}	6×10^4	No
Asteroidal bodies	1.8–3.8	180	2×10^{22}	0.04	No
Meteoroids	<10	100–275	10^{19}	0.005	No
Interstellar dust	≥ 2	<200	2×10^{-21} m^{-3}	0.004–0.02	Yes
Zodiacal light	≤ 3.5	275	10^{19}–10^{20}	25	No
Hypothetical cloud	60	30	$10^{26} a$(cm)	14[a]	Yes

[a] Assumed equal to the residual isotropic emission (eq. [1] and Fig. 1*a*).

values of d if the cloud consists of dust particles with an $n = 2$ emissivity law instead. However, the figure shows that a cloud of dust particles with radii $\lesssim 0.1$ cm is unstable against Poynting-Robertson (P-R) drag and interactions with the ISM. Only a cloud consisting of objects larger than ~ 1 cm located between ~ 5 and 150 AU would be stable against local and ISM forces. A cloud with a temperature of 30 K located at 60 AU could give rise to *all* of the residual isotropic emission observed in the DIRBE bands provided its mass is $\gtrsim 10^{26}\, a$(cm) g. The distance and temperature of the cloud are similar to those expected for the Kuiper Belt. However, the Kuiper Belt is a disk or ring, and cannot produce an isotropic emission component. Solar system components that can produce an isotropic foreground, such as the inner and outer Oort clouds, are too distant and their emission is too faint to contribute significantly to the DIRBE 140 or 240 μm emission. Table 1 is adapted from Leinert (1996) and shows the possible 240 μm contributions from known solar system components. The hypothetical cloud considered above is the last entry in the table, marked "hypothetical cloud."

Such hypothetical clouds may have been observationally detected around main-sequence stars by the *IRAS* satellite. From detailed statistical analysis of the *IRAS* survey data of main-sequence stars located within ~ 25 pc of the Sun, Aumann (1988) suggested that the presence of cool shells around A, F, and G stars is the rule, rather than the exception. Further analysis (Aumann & Good 1990) suggested that typical cloud temperatures are 20–38 K and cloud radii are 100–150 AU, not unlike the properties of the hypothetical cloud required to produce the residual isotropic emission. The presence of these shells was inferred from the 60 μm excess in the colors of these stars, and *IRAS* lacked the spatial resolution to determine the geometry of the cloud. In the following we show that a spherical cloud at these distances will be disrupted by collisions and probably settle into a disk. The *IRAS* data are therefore probably indicative of cool disks, rather than spherical shells, around these stars. This has been directly confirmed in some cases (e.g., β Pic).

Adopting centimeter-sized objects as the cloud constituent particles, it is easy to show that the hypothetical cloud lifetime against internal collisions is significantly smaller than the age of the solar system. The collisional lifetime is roughly given by $(n\,\Delta v \sigma)^{-1}$, where n is the number density of cloud particles, Δv their relative velocities or internal velocity dispersions, and σ their geometrical cross section. The collisional lifetime is therefore proportional to the optical path length $l \equiv \tau/(n\sigma)$, and can therefore be related to the residual intensity I_ν it is required to produce by

$$\tau_{\rm coll} = \frac{B_\nu(T) l}{I_\nu\, \Delta v}\,. \tag{5}$$

Adopting a cloud distance d of 60 AU, we find that the orbital velocity v is ~ 4 km s^{-1}. Perturbative forces due to other solar system objects will cause particle orbits to cross, so that $\Delta v \approx 4$ km s^{-1}. For $T = 30$ K, and a shell thickness l equal to 1/10 of the cloud's heliocentric distance, the collisional lifetime is $\sim 3 \times 10^6$ yr, considerably smaller than the lifetime of the solar system. This conclusion is not significantly altered if we adopt different cloud distances or particle sizes within the range of distances allowed in Figure 2. The internal collisions will grind the cloud particles into finer dust particles, causing them to either spiral into the Sun or settle into a disklike configuration.

Having ruled out any *stable isotropic* cloud as a source of the residual 140 and 240 μm emission, we still need to consider the possible existence of a cloud of particles that is continually replenished (*as is the main interplanetary dust cloud*) as a viable source for the emission. Figure 1*b* and Table 1 show that the inner Oort cloud is positioned at the correct distance and has a suitable isotropic geometry and mass for being a potential source of the cloud. However, the transport of particles from this location to a distance of ~ 100 AU by P-R drag will take over 10^{12} yr, making any causal relation between the two clouds highly improbable. Other solar system components are even less likely to be the source of the cloud since they are either farther away or have too little mass. We therefore conclude that no existing solar system component can possibly replenish the mass loss from a cloud sufficiently massive to produce significant 140 and 240 μm emission.

2.2. *A Galactic Isotropic Emission Component*

The temperature limits discussed above eliminate the possibility that a significant portion of the 240 μm emission arises from warm and hot Galactic sources such as white or brown dwarfs. The only significant Galactic contribution to the 240 μm residual must come from interstellar dust with a temperature less than 30 K, assuming an emissivity index of $n = 2$. By itself, this requirement can be easily met, since the 140–240 μm color temperature of the residual emission is ~ 16.5 K, which is quite close to the temperature derived for dust associated with H I in the outer Galaxy (Sodroski et al. 1997; Dwek et al. 1997). However, the isotropy of the residual emission suggests that any significant contribution to the 240 μm residual emission must come from a large (radius $R \gg 8.5$ kpc), roughly spherical, shell of material. A smaller, or centrally condensed cloud would produce observable brightness variations of the emission across the sky. It is very likely that stellar radiation pressure or correlated supernova explosions can expel dust into the halo of our Galaxy (Ferrara et al. 1991). However, the expelled dust is likely to be patchy and associated with Galactic fountains, chimneys, or clusters of OB stars, and therefore not likely to give rise to an isotropic emission component. Furthermore, the required mass of expelled dust is too high to be of Galactic origin. If the entire 240 μm residual intensity is assumed to arise from a Galactic dust shell, then its mass is $M_{\rm dust} \approx 10^5 R^2\, M_\odot$ (see eq. [4]), where R is the radius of the shell in kpc. Adopting a radius of 15 kpc yields a total mass of $\sim 2 \times 10^7\, M_\odot$ of dust and $\sim 3 \times 10^9\, M_\odot$ of gas (assuming a dust-to-gas mass ratio of $Z_d = 0.007$). This mass of gas is nearly as large as the mass of the gas in the disk of the Galaxy (e.g., Sodroski et al. 1997). This large gas mass suggests that it is very unlikely that the residual emission arises from an unmodeled Galactic ISM component.

The dust required to produce an isotropic Galactic background component exhibits very similar characteristics to the dust tentatively detected by Zaritsky (1994) to be present in the halo of the galaxies NGC 2835 and NGC 3521. At a distance of 15 kpc, the mass surface density of the hypothetical Galactic dust shell must be about 10^{-6} g cm^{-2}, giving a visual optical depth of ~ 0.05 for a Galactic extinction law. Such a halo of dust particles will produce a $B-I$ color excess of about 0.07, similar to the extinction observed by Zaritsky (1994) through the halo of the two

galaxies at a distance of 60 kpc from their center. These observations are taken as preliminary evidence that galactic halos may be dusty even at those radii. However, the extinction observed by Zaritsky was along the major axis of these galaxies and can therefore be only considered as evidence for the presence of dust in an extended disk. The mass of dust required to be in the disk and to produce the observed color excess will therefore be significantly less than the mass of Galactic halo dust required to produce the intensity of the isotropic residual IR emission. The presence of a dusty disk component in our Galaxy, with characteristics similar to the two galaxies observed by Zaritsky, can therefore not be ruled out; however, such dust cannot produce an isotropic emission component.

We conclude from the considerations of this section that the residual isotropic 140 and 240 μm radiation measured by the DIRBE and, by inference, the detections measured by the FIRAS as well, are most likely of extragalactic origin.

3. LIMITS ON THE EBL AT 100 μm

After the removal of foreground emission, the DIRBE instrument detected a positive residual at 100 μm with a value of $\nu I(\nu) = 21.9 \pm 6.1$ nW m^{-2} sr^{-1} (Paper I). However, this residual emission is not isotropic, a strict requirement for the extragalactic background. Hauser et al. (1998) therefore claimed a 95% confidence level upper limit of $\nu I(\nu) < 34$ nW m^{-2} sr^{-1} at this wavelength. A model-dependent lower limit of 3.9 nW m^{-2} sr^{-1} was derived from *IRAS* galaxy counts (Hacking & Soifer 1991). However, the positive detections at 140 and 240 μm can be used to derive a largely model-independent lower limit on the IR intensity that must be present at 100 μm.

Infrared lines, most notably the [C II] 158 μm line, will not contribute significantly to the EBL detected in the DIRBE 140 and 240 μm bands. Because of the broad DIRBE spectral response, even the Galactic C^+ line does not contribute significantly to the energy received in the 140 μm band (Wright et al. 1991). Emission from different redshifts will further reduce the relative line contribution to the in-band flux, since the line can originate from only a limited range of redshifts, whereas no such restriction applies to the continuum. The EBL detected in the DIRBE 140 and 240 μm bands most likely consists largely of emission from dust heated by X-ray, UV, or optical photons, regardless of their origin (whether stellar or nonthermal). The same physical process that produces the 140 and 240 μm continuum emission must contribute to a signal at 100 μm as well. The exact value of this contribution is, of course, model dependent. However, the steepest possible drop-off from 140 to 100 μm is the Wien exponential corresponding to the coldest dust spectrum that is consistent with the 140 and 240 μm detections. The coldest dust spectrum is obtained by fitting the DIRBE detections with a blackbody modified by a ν^2 emissivity law. Any more realistic spectrum consisting of the contribution of emission from dust at different temperatures and redshifts will give rise to a broader spectrum and an increased 100 μm intensity.

A fit to the nominal values of the DIRBE detections gives a dust temperature of about 15 K and a lower limit of $\nu I(\nu) = 14$ nW m^{-2} sr^{-1} at 100 μm. To assess the statistical significance of any lower limit, we calculated the 100 μm intensity for all possible $[I(140\ \mu\text{m}) \pm 2\ \sigma, I(240\ \mu\text{m}) \pm 2\ \sigma]$ combinations, assuming partially (50%) correlated errors. The results show that $\nu I(\nu) > 5$ nW m^{-2} sr^{-1} with a larger than 95% probability. Hence, under the assumption that most of the 140 and 240 μm residual emission is thermal emission from dust, we adopt the following conservative lower and upper limits on the EBL at 100 μm:

$$5 < \nu I(\nu)[\text{nW m}^{-2}\ \text{sr}^{-1}] < 34 \quad \text{at } 100\ \mu\text{m} . \tag{6}$$

4. THE EXTRAGALACTIC BACKGROUND LIGHT FROM NUCLEOSYNTHESIS

The total integrated extragalactic background light detected by the DIRBE and FIRAS instruments in the 140–1000 μm wavelength interval is ~ 16 nW m^{-2} sr^{-1}. In this section we compare the integrated background with that expected from the stellar production of helium and metals. Given a cosmic star formation rate, we calculate the energy density in a comoving volume element as a function of redshift. The observed EBL consists of the cumulative redshifted radiation from these volume elements.

The differential bolometric flux $d\mathscr{F}$ received from a comoving volume element dV_c located at redshift z, with a comoving luminosity density $\epsilon(z)$ is given by (e.g., Kolb & Turner 1990)

$$d\mathscr{F} = \frac{\epsilon(z) dV_c(z)}{4\pi d_L^2(z)} , \tag{7}$$

where $d_L(z)$ is the luminosity distance to the volume element and

$$\frac{dV_c}{4\pi d_L^2} = \left(\frac{\delta\Omega}{4\pi}\right) \left|\frac{c\,dt}{dz}\right| \frac{dz}{1+z} . \tag{8}$$

The frequency-integrated intensity I received from a distribution of sources within the solid angle $\delta\Omega$ is given by the integral

$$I = \left(\frac{c}{4\pi}\right) \int_0^{z_*} \epsilon(z) \left|\frac{dt}{dz}\right| \frac{dz}{1+z} , \tag{9}$$

where z_* represents the redshift when stars first turned on, and

$$\begin{aligned} |\,dt/dz\,|^{-1} &= H_0(1+z)[(1+z)^2(1+\Omega_0 z) - z(2+z)\Omega_\Lambda]^{1/2} \\ &\equiv H_0\,\mathscr{G}(\Omega_0, \Omega_\Lambda, z) , \end{aligned} \tag{10}$$

where H_0 is the Hubble constant, $\Omega_0 \equiv \rho_o/\rho_c$ is the present mass density of the universe normalized to the critical density $\rho_c = 4.70 \times 10^{-30}\ h_{50}^2$ g cm^{-3}, $\Omega_\Lambda \equiv \Lambda/3H_0^2$ is the dimensionless cosmological constant, and h_{50} is the value of H_0 in units of 50 km s^{-1} Mpc^{-1}.

It is useful to define a dimensionless radiative energy density parameter Ω_R as

$$\Omega_R \equiv \left(\frac{4\pi}{c}\right) \frac{I}{\rho_c c^2} , \tag{11}$$

where

$$\rho_c c^2 = 4.23 \times 10^{-9}\ h_{50}^2\ \text{ergs cm}^{-3} . \tag{12}$$

Numerically, the parameter Ω_R is related to the integrated EBL intensity I as

$$\Omega_R = 1.0 \times 10^{-7} I(\text{nW m}^{-2}\ \text{sr}^{-2}) h_{50}^{-2} . \tag{13}$$

To calculate I, we need to know the value of the luminosity density ϵ as a function of redshift z, or epoch t_z measured since the epoch t_*, when stars first turned on. Assuming that the total radiant background arises from

energy released by nucleosynthesis, the value of ϵ is related to the cosmic star formation rate $\psi(t)$ (in stars yr^{-1} Mpc^{-3}) as

$$\epsilon(t_z) = \int_{t_*}^{t_z} dt\psi(t) \int_{M_{\rm low}}^{M(t')} L(m, t')\phi(m)dm \ , \qquad (14)$$

where $L(m, t')$ is the luminosity of a star of initial main-sequence mass m at time $t' = t_z - t$, $\phi(m)$ is the stellar mass spectrum, normalized to unity in the $(M_{\rm low}, M_{\rm up})$ mass interval, and $M(t')$ is the initial main-sequence mass of a star with a lifetime $t' = t_z - t$. Equation (14) was evaluated using the stellar evolutionary tracks of Bressan et al. (1993) and takes the delayed release of stellar energy into account. Consequently, even if all stars were formed in an instantaneous burst, their energy output will be spread out over their respective lifetimes.

The dependence of the cosmic star formation rate on redshift can be inferred from the variation of metal abundances in QSO absorption-line systems (e.g., Pettini et al. 1997), from the consumption of H I in damped Lyα systems (Pei & Fall 1995, hereafter PF95), or from photometric studies of the UV output of galaxies at various redshifts (e.g., Madau et al. 1996, and references therein). Applying the UV and blue dropout techniques to galaxies in the Hubble deep field (HDF), Madau et al. (1996) derived star formation rates for $z = 2.75$ and 4.0. Figure 3 depicts several cosmic star formation rates as a function of redshift. The UVO curve represents the UV-optically derived cosmic star formation rate compiled by Madau et al. (1996) as recently revised by Madau, Pozetti, & Dickinson (1998, hereafter MPD98). The revised SFR is somewhat higher that the previous estimate of Madau et al. (1996), peaking at a somewhat higher redshift of $z \approx 1.4$. The PFI and PFC curves represent the cosmic SFR in, respectively, the infall and closed box cosmic chemical evolution models of PF95. Figure 1*d* in PF95 depicts the *net* mass consumption rate due to star formation, which needs to be divided by $(1 - R)$, where R is the average fraction of the initial stellar mass that is returned back to the ISM over the stellar lifetime. In deriving the stellar birthrate we assumed this fraction is constant and equal to 0.30. For a Salpeter stellar mass spectrum, $\phi(m) \sim m^{-2.35}$, and $(M_{\rm low}, M_{\rm up}) = (0.1\ M_\odot, 120\ M_\odot)$, the average stellar mass is $0.35\ M_\odot$, so the stellar birthrate, ψ (in yr^{-1} Mpc^{-3}), is related to the mass consumption rate due to star formation, ρ_*, as

$$\psi(\text{yr}^{-1}\ \text{Mpc}^{-3}) = 2.9 \times \rho_*(M_\odot\ \text{yr}^{-1}\ \text{Mpc}^{-3}) \ . \qquad (15)$$

The star formation rate derived from UV and optical observations is, in principle, a lower limit on the cosmic SFR. Ultraviolet and optical surveys systematically underestimate the star formation rate, since a significant fraction of the UV-optical stellar output can be absorbed and reradiated at IR wavelengths by dust. The magnitude of the discrepancy is, however, still controversial. Rowan-Robinson et al. (1997) argued that *ISO* observations of the HDF suggest that the star formation rate remains constant at $z \gtrsim 1.5$, instead of decreasing. In this scenario the UV observations of the HDF represent only a fraction of the actual star formation activities at these high redshifts. The actual SFR may have been underestimated at lower redshifts as well. Figure 4 depicts the cosmic luminosity density, calculated using equation (14), as a function of redshift for the various cosmic star formation rates depicted in Figure 3. The various star formation scenarios give somewhat different local luminosity densities that are summarized and compared to the observations in Table 2.

Integration of the luminosity density over redshift (eq. [9]) for $\Omega_0 = 1$ and $\Omega_\Lambda = 0$ gives

$$\begin{aligned} I(\text{nW m}^{-2}\ \text{sr}^{-1}) &= 30 \quad \text{for UVO} \ , \\ &= 91 \quad \text{for PFI} \ , \\ &= 41 \quad \text{for PFC} \ . \end{aligned} \qquad (16)$$

The positive detection of the EBL by the *COBE* therefore accounts for about 20%–50% of the expected EBL associated with the energy release from nucleosynthesis, depending on the adopted cosmic SFR. The EBL was also recently detected at UV-optical wavelengths by Bernstein (1997, see also Bernstein, Freedman, & Madore (1998). A lower limit on the EBL was set at $\lambda = 0.36$, 0.45, 0.67 (Pozzetti et al. 1998) and at 2.2 μm (Gardner 1996) by calculating the contribution of discrete objects. These lower limits suggest an

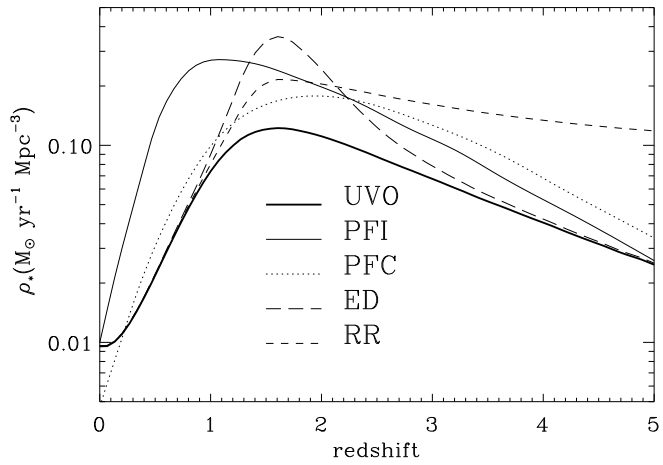

FIG. 3.—Cosmic star formation rate, $\rho_*(z)$, as a function of redshift. Shown are rates inferred from UV and optical observations, recently compiled by MPD98 (*bold solid line*; labeled UVO), and the rates inferred for various star-forming scenarios in the cosmic chemical evolution model of PF95: the infall model (*thin solid line*; PFI), and the closed box model (*dotted line*; PFC). The long-dashed line (labeled ED) represents a cosmic star formation rate constructed to fit the EBL intensities detected by *COBE*. The short-dashed line (RR) represents a cosmic star formation rate with an excess of sources at high redshifts, similar to that suggested by RR97 to account for the excess IR galaxies observed by *ISO* in the HDF.

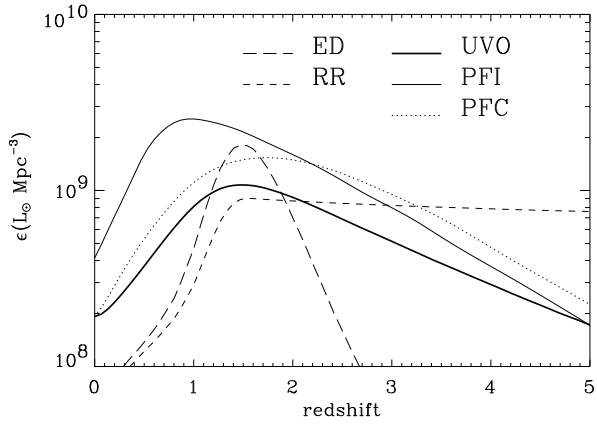

FIG. 4.—Cosmic luminosity density, $\epsilon(z)$, calculated for the various star formation histories depicted in Fig. 3. The ED and RR curves represent the *excess* luminosity density associated with the ED and RR star formation rates, over that of the UVO model (*bold solid line*).

TABLE 2

SELECT MODEL OUTPUT PARAMETERS[a]

Quantity	UVO	PFI	PFC	Observed
I [nW m^{-2} sr^{-1}]	30	91	41	28 [b]
$\epsilon(z=0)$ [$L_\odot$ Mpc^{-3}]	1.9×10^8	4.1×10^8	1.9×10^8	$(1.8 \pm 0.7) \times 10^8$ [c]
ϵ(4400 Å, $z=0$) [W Hz^{-1} Mpc^{-3}]	2.0×10^{19}	3.2×10^{19}	1.8×10^{19}	$(2.0 \pm 0.8) \times 10^{19}$ [d]
$\epsilon_{IR}(z=0)$ [$L_\odot$ Mpc^{-3}]	5.0×10^7	6.3×10^7	4.5×10^7	5.3×10^7 [c]
$\tau(V)$	0.27	0.20	0.35	...

[a] Models are explained in § 4 of the text.
[b] Observed in the 0.36–2.2 and 140–5000 μm wavelengths interval.
[c] See § 5.2 of the text.
[d] Lilly et al. 1996.

EBL intensity $\gtrsim 12$ nW m^{-2} sr^{-1} in the 0.36 to 2.2 μm wavelength interval, which combined with the *COBE* detections gives an *observed* EBL intensity in the 0.36–2.2 and 140–5000 μm wavelength intervals in excess of ~ 28 nW m^{-2} sr^{-1}. This value is similar to the EBL intensity predicted by the UVO cosmic SFR. The UVO star formation rate therefore leaves no room for any expected EBL emission in the 2.2 to 140 μm wavelength region, indicating that the UV-optically determined SFR underestimates the actual rate of star formation in the universe.

Most of the energy radiated by stars is liberated during the transmutation of protons into helium and heavier elements. The radiative energy density parameter, Ω_R, can therefore be related to Ω_*, the fraction of the total critical mass density that has been processed through stars (BCH86, Peebles 1995). The value of Ω_* depends on details of the chemical evolution of a comoving volume element in the universe (Pei & Fall 1995). For simplicity we will assume that all the elements were instantaneously formed at some epoch corresponding to some redshift z_e. The intensity of the EBL consists of the energy released from the production of He that was not further processed into heavier elements and of the energy released by the production of elements heavier than He. It can be written as

$$I = \left(\frac{c}{4\pi}\right) \frac{\Omega_* \rho_c c^2}{1+z_e} (\eta_Y \Delta Y + \eta_Z Z_*) . \quad (17)$$

The parameter $\eta_Y = 0.0072$ is the energy conversion efficiency for the nuclear energy generating reactions $4p \rightarrow {}^4$He, $\eta_Z = 0.0078$ is that for the $12p \rightarrow {}^{12}$C reaction that leads to the production of metals, Z_* is the current mass fraction of matter that was converted into metals, and ΔY is the net enrichment in the ^{4}He mass fraction due to stellar processing. For $Z_* = Z_\odot = 0.02$, the solar metallicity, and $\Delta Y = 0.04$, which is the difference between the solar ($Y = 0.28$) and the primordial ($Y = 0.24$) ^{4}He mass fraction, most of the contribution to the EBL is due to the net enrichment of He in the universe and

$$\Omega_* = 6.3 \times 10^{-3}\, h_{50}^{-2} \left(\frac{\Omega_R}{28 \times 10^{-7}}\right)(1+z_e) , \quad (18)$$

where Ω_R is normalized to the *observed* radiative energy density parameter of the EBL.

To put this derived value of Ω_* in perspective, we note that a strict upper limit on Ω_* is provided by the baryonic mass-density parameter Ω_{BBN} derived from big bang nucleosynthesis (BBN) arguments:

$$\Omega_* h_{50}^2 < \Omega_{BBN} h_{50}^2 \approx 0.044\text{–}0.15 , \quad (19)$$

where we adopted a conservative range of values for $\Omega_{BBN} h_{50}^2$ (Kolb & Turner 1990; Steigman, Hata, & Felten 1998). The parameter Ω_{BBN} represents a strict upper limit on Ω_*, since a fraction of the baryonic matter is locked up in low-mass stars that never cycled their nucleosynthetic products back to the interstellar medium. An approximate lower limit on Ω_* can be derived from the amount of luminous matter currently locked up in stars:

$$\Omega_* > \Omega_{LUM} \equiv \epsilon_B \langle M/L_B \rangle / \rho_c \approx 1.4 \times 10^{-3}\, h_{50}^{-1} , \quad (20)$$

where the numerical value was obtained for a local blue luminosity density, $\epsilon_B = 7.9 \times 10^6\, h_{50}\, L_\odot$ Mpc^{-3} (Lilly et al. 1996), presented here in units of the bolometric solar luminosity $L_\odot = 3.826 \times 10^{33}$ ergs s^{-1}. We also used a conservative lower limit of $\langle M/L_B \rangle = 14\, M_\odot/L_\odot$ (in bolometric $L_\odot$) derived from stellar population models of Larson & Tinsley (1978). So we find the consistent relationships

$$\begin{aligned} \Omega_{LUM} &\approx 1.4 \times 10^{-3}\, h_{50}^{-1} \\ &< \Omega_* \approx 0.013\, h_{50}^{-2} \frac{1+z_e}{2} \\ &< \Omega_{BBN} \lesssim 0.15\, h_{50}^{-2} , \end{aligned} \quad (21)$$

where we have included in Ω_R the UV and near-IR contribution to the EBL. The average redshift for metal production weighted by the integrand of equation (9) is $z_e = 1.0$, giving $\Omega_* \approx 0.013\, h_{50}^{-2}$ for the observed intensity of the EBL. This value of Ω_* is consistent with the range of (0.044–0.15) h_{50}^{-2} required for big bang nucleosynthesis. The UV to near-IR and the *COBE* 140–5000 μm wavelength detection therefore imply that at least $\sim 10\%$, and possibly as much as $\sim 30\%$ of the total baryonic mass density inferred from big bang nucleosynthesis was processed in stars into heavier elements. In the following we examine the consistency of the *COBE* background measurements with the expected spectrum of the EBL.

5. SPECTRAL ENERGY DISTRIBUTION OF THE EXTRAGALACTIC BACKGROUND LIGHT

5.1. *Model Description*

Numerous models have been constructed by various authors to predict the intensity and spectrum of the EBL using observational constraints and theoretical models for the evolution of galaxies. Pioneering work in this field was conducted by Partridge & Peebles (1967), Harwit (1970), BCH86, BCH91, and Negroponte (1986, and references therein). A more complete set of references to more recent work can be found in various papers in the proceedings of the conference Unveiling the Cosmic Infrared Background (Dwek 1996).

The specific intensity $I(\nu_0)$ of the EBL at the observed frequency ν_0 is obtained by integrating the spectral luminosity density, $\epsilon(\nu, z)$, from the comoving volume elements at z, over redshifts:

$$I(\nu_0) = \left(\frac{c}{4\pi}\right) \int_0^{z_*} \epsilon(\nu, z) \left|\frac{dt}{dz}\right| dz \,, \tag{22}$$

where $\nu = \nu_0(1 + z)$ is the frequency in the rest frame of the comoving volume element.

At each redshift, the spectral luminosity density can be written as the following sum:

$$\epsilon(\nu, z) = \epsilon_s(\nu, z) + \epsilon_d(\nu, z) \,, \tag{23}$$

where $\epsilon_s(\nu, z)$ and $\epsilon_d(\nu, z)$ are, respectively, the attenuated starlight and the dust contribution to the spectral luminosity density. The total, unattenuated, spectral luminosity density from starlight, $\epsilon(\nu, z)$, can be calculated from population synthesis models. Given the evolution of the cosmic SFR as a function of time, the stellar mass spectrum, stellar evolutionary tracks and nucleosynthesis yields, and stellar atmosphere models as a function of metallicity, the spectral luminosity density can be uniquely determined as a function of time (e.g., Charlot, Worthey, & Bressan 1996). The redshift dependence of $\epsilon(\nu, z)$ is, to first order, independent of the cosmological parameters H_0, Ω_0, and Ω_Λ, if the cosmic SFR is observationally determined or constrained as a function of redshift. However, a second order dependence of the spectral luminosity density on the cosmological parameters enters into the model through the finite stellar lifetimes in the population synthesis models.

Significantly more complicated is the determination of the fraction of the stellar spectral energy distribution that is absorbed by dust and reradiated at IR wavelengths. Many different approaches have been applied to the problem. Lonsdale (1995, 1996) grouped the various methods into two major categories: backward and forward evolution models. Cosmic chemical evolution models (Pei & Fall 1995) can be regarded as a third, distinct, category. Backward evolution models adopt the currently observed galaxy luminosity function and spectral energy distribution (see § 5.2 below), and translate them backward in time. Notable models in this category were constructed by Hacking & Soifer (1991), Beichman & Helou (1991), and more recently by Malkan & Stecker (1998). Forward evolution models evolve various galactic systems, such as elliptical, spiral, and starburst galaxies, from an initial redshift z_* forward in time using population synthesis and chemical evolution models (e.g., Rocca-Volmerange & Fioc 1996; Franceschini et al. 1996, 1997; Guiderdoni et al. 1997). In these models, the fraction of absorbed starlight is determined by simple radiative transfer models, and the reradiated IR emission is taken as a combination of spectra representing dusty H II, H I, and molecular cloud regions. These models have been quite successful in reproducing the UV to far-IR spectra of various types of galaxies. Cosmic chemical evolution models adopt a more global approach than forward evolution models by generalizing standard Galactic chemical evolution models (e.g., Tinsley 1980) to the universe as a whole. The cosmic SFR in these models is constrained by the diminution of H I column density as a function of redshift. Recently, Fall, Charlot, & Pei (1996) used this approach in conjunction with population synthesis and dust and chemical evolution models to predict the EBL at UV to far-IR wavelengths. Unique to these models is the fact that the gas opacity (and hence the thermal dust emission) at each redshift is constrained by the observed obscuration of quasars.

In this paper we calculate the EBL spectrum using a combination of all three approaches. Given a cosmic star formation rate, the unattenuated stellar spectral luminosity density, $\epsilon(\nu, z)$, at each redshift is calculated using detailed population synthesis models. For these calculations, we adopt the stellar evolutionary tracks of Bressan et al. (1993), Kurucz stellar atmosphere models for a solar metallicity composition, and a Salpeter stellar mass spectrum in the 0.1–120 $M_\odot$ mass interval. The attenuated stellar spectral luminosity density at each redshift is given by

$$\epsilon_s(\nu, z) = [1 - P_{\rm abs}(\nu)] \times \epsilon(\nu, z) \,, \tag{24}$$

where $P_{\rm abs}(\nu)$ is the probability that a photon of frequency ν is locally absorbed by the ambient dust. In this model we take $P_{\rm abs}(\nu) = 1 - \exp\,[-\tau_{\rm abs}(\nu)]$, independent of redshift, where $\tau_{\rm abs}$ is the dust absorption opacity, calculated for an average Galactic interstellar extinction law normalized to some value in the V band, with a wavelength independent albedo of 0.5 (e.g., Dwek 1997). Note that in spite of the fact that $P_{\rm abs}(\nu)$ is independent of redshift, the fraction of starlight that is converted to IR emission is a redshift dependent quantity, since the spectrum of the stellar luminosity density evolves with time. We further assume that the spectrum of the emerging IR emission is given by the luminosity function–averaged spectrum of the *IRAS* galaxies (see § 5.2 and Fig. 5). The spectral luminosity density of the dust at z can then be expressed in terms of its *local* spectral luminosity density, $\epsilon_d(\nu, 0)$, as

$$\epsilon_d(\nu, z) = \epsilon_d(\nu, 0) \frac{\int P_{\rm abs}(\nu)\epsilon(\nu, z)d\nu}{\int P_{\rm abs}(\nu)\epsilon(\nu, 0)d\nu} \,. \tag{25}$$

The adopted prescription for calculating the IR background is admittedly simplified. The cosmic SFR represents a statistical average over many galactic systems, each possessing a complex star formation history that can be studied with nonlinear multipopulation models (see review by Shore & Ferrini 1995). A more realistic approach to calcu-

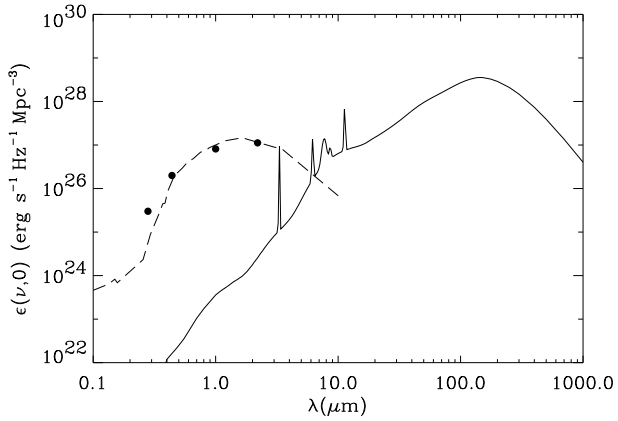

FIG. 5.—Local spectral luminosity density at 0.28, 0.44, and 1.0 μm (Lilly et al. 1996) and at 2.2 μm (Gardner et al. 1997) indicated by solid circles is compared to the starlight emitted by an average spiral galaxy (Schmitt et al. 1997; *dashed line*). The heavy solid curve represents the average IR spectrum of *IRAS* galaxies. Its derivation is described in § 5.2 of the text.

lating galactic spectra should include the effects of the evolution of the dust abundance and composition, as well as the clumpiness and fractal nature of the interstellar medium on the photon escape probability (Fall et al. 1996; Dwek & Városi 1996; Dwek 1998; Witt & Gordon 1996).

5.2. *The Local UV to Far-IR Spectral Luminosity Distribution*

The values of $\epsilon_s(\nu, z)$ and $\epsilon_d(\nu, z)$ at $z = 0$ can be determined from observations of the local luminosity density in the various visual, near-, and far-IR bands. Using the Canada-France Redshift Survey, Lilly et al. (1996) estimated local luminosity densities of $\epsilon(\nu, 0) = 3.0 \times 10^{25}$, 2.0×10^{26}, and 8.1×10^{26} ergs s^{-1} Hz^{-1} Mpc^{-3} at $\lambda = 0.28$, 0.44, and 1.0 μm, respectively, for $h_{50} = 1$. At 2.2 μm, Gardner et al. (1997) give a value of 1.1×10^{27} ergs s^{-1} Hz^{-1} Mpc^{-3}. The stellar spectral luminosity density can be well represented by the spectrum of an average spiral or elliptical galaxy (Schmitt et al. 1997). Normalizing the spectrum of the average spiral galaxy to the local spectral luminosity density yields an integrated luminosity density in the 0.1–10 μm wavelength interval of $(1.30 \pm 0.7) \times 10^8$ $L_\odot$ Mpc^{-3}, the error reflecting the 1 σ uncertainties in the determination of the B-band luminosity density, including the value derived by MPD98 from the local B-band luminosity function determined by Ellis et al. (1996). Figure 5 depicts the data of Lilly et al. (1996) and Gardner et al. (1997) and the SED of an average spiral galaxy (Schmitt et al. 1997, Table 6) normalized to fit the observed spectral luminosity density at $\lambda \lesssim 3$ μm.

At wavelengths above $\sim$5–10 μm, the spectral luminosity density is dominated by thermal emission from dust and is represented by that of *IRAS* galaxies. In general, any galactic dust spectrum can be represented by a combination of three emission components: (1) a hot dust component, as one would expect from dust in H II regions; (2) a warm dust component, as one would expect from dust in the diffuse H I gas and heated by the general interstellar radiation field; and (3) a cold dust component, arising from dust in molecular clouds.

IRAS observations of IR bright galaxies show a systematic variation of IR colors with luminosity, characterized by decreasing $I(12\ \mu\text{m})/I(25\ \mu\text{m})$, and increasing $I(60\ \mu\text{m})/I(100\ \mu\text{m})$ flux ratios, with increasing IR luminosity (Soifer & Neugebauer 1991). This trend can be used to construct luminosity-dependent spectral templates of the *IRAS* galaxies using a linear combination of the three spectral dust components. In practice, the *IRAS* color-color trend can be reproduced with just the H II and H I dust components. Figure 6 shows the H II and H I spectral dust components, arbitrarily normalized. The H II spectrum represents that of typical Galactic H II regions such as Orion (Wall et al. 1996). The H I spectrum represents the model fit to the DIRBE observations of the diffuse ISM, consisting of the emission from a mixture of polycyclic aromatic hydrocarbons (PAHs), graphite, and silicate grains, stochastically heated by the ambient radiation field (Dwek et al. 1997). Also shown in the figure is the spectrum of Arp 220, an interacting ultraluminous IR galaxy (ULIRG) obtained by Klaas et al. (1997) using the *Infrared Space Observatory* (*ISO*) satellite. Arp 220 is somewhat hotter than other interacting systems (Klaas et al. 1997), so the H II spectrum adopted in this paper is representative of a prototypical ULIRG. Table 3 shows the relative contribution of the H II

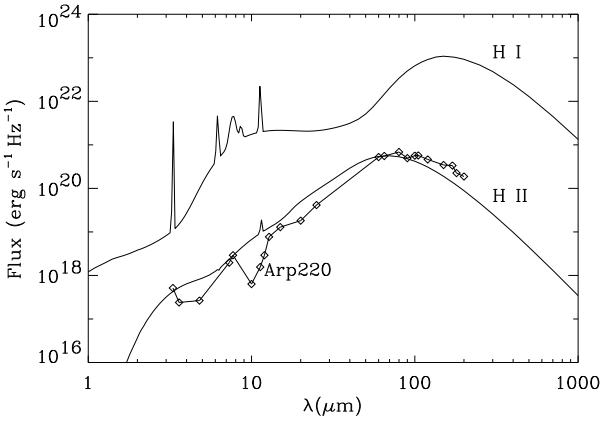

FIG. 6.—Arbitrarily normalized spectral luminosity of the H II and H I dust components that were used to construct the *IRAS* galaxy spectra. The H II spectrum represents a somewhat hotter version of the Orion spectrum obtained from the DIRBE data (Wall et al. 1996). The diamonds depict the spectrum of Arp 220 obtained with the *ISO* satellite (Klaas et al. 1997), arbitrarily normalized for comparison with the H II spectrum. The figure shows that the H II spectrum is a reasonable representation of that of interacting galaxies. The H I spectrum represents the model fit of Dwek et al. (1997) to the DIRBE observations of the IR emission from the diffuse H I component of the Galaxy.

TABLE 3

DUST EMISSION COMPONENTS OF *IRAS* GALAXIES AND THEIR AVERAGE FLUX RATIOS[a]

log ($L_{IR}/L_\odot$) (1)	f(H II) (2)	f(H I) (3)	$S_\nu(12\ \mu\text{m})/S_\nu(25\ \mu\text{m})$ (4)	$S_\nu(60\ \mu\text{m})/S_\nu(100\ \mu\text{m})$ (5)
<9.5	0.27	0.73	0.69	0.36
9.75	0.28	0.72	0.68	0.37
10.25	0.34	0.66	0.59	0.42
10.75	0.45	0.55	0.46	0.51
11.25	0.61	0.39	0.32	0.66
11.75	0.78	0.22	0.22	0.84
12.0	0.88	0.12	0.17	0.96
13.0	1.0	0.0	0.13	1.11

[a] The parameters f(H II) and f(H I) are, respectively, the luminosity-dependent fractional contribution of the H II and H I dust spectra (shown in Fig. 6) to the spectra of the *IRAS* galaxies. The flux ratios in cols. (4) and (5) are the derived flux ratios of the galaxies and should be compared with the mean observed values given in Table 5 of Soifer & Neugebauer 1991. The agreement is *exact* for the 12 to 25 μm flux ratio and deviates from the 60 to 100 μm flux ratio by less than $\sim$10%. Galaxies with $L_{IR} = 10^{13}$ $L_\odot$ are represented by a pure H II spectrum.

and H I components to the IR spectra of various *IRAS* galaxies. The mean observed colors of the *IRAS* galaxies as a function of their luminosity were taken from Table 5 of Soifer & Neugebauer (1991). Galaxies with $L_{IR} = 10^{13}\ L_\odot$ were represented by a pure H II spectrum. Figure 7 depicts the template spectra of these various galaxies. The spectra of the more luminous galaxies peak at shorter wavelengths, due to the increased contribution to their spectrum of the H II component, relative to that of the H I.

An average local IR spectrum was derived by averaging the individual galactic spectral templates over the *IRAS* galaxy luminosity function $\Phi(L)$. This luminosity function (LF) was originally derived by Soifer et al. (1987). Here we use the fit of Beichman & Helou (1991), adjusted for a value of $H_0 = 50\ \mathrm{km\ s^{-1}\ Mpc^{-1}}$:

$$\Phi(L)dL = \Phi_*\left(\frac{L}{L_0}\right)^{\beta}\left(\frac{dL}{L_0}\right) \quad \text{for } L \le L_0\ ,$$

$$= \Phi_*\left(\frac{L}{L_0}\right)^{\gamma}\left(\frac{dL}{L_0}\right) \quad \text{for } L \ge L_0\ , \qquad (26)$$

where L represents the IR luminosity of the galaxies, $L_0 = 5.65 \times 10^{10}\ L_\odot$, $\Phi_* = 3.0 \times 10^{-4}\ \mathrm{Mpc^{-3}}$, $\beta = -1.65$, and $\gamma = -3.31$. An IR luminosity range of 3.2×10^8 to 1×10^{13} $L_\odot$ was adopted in all calculations.

The local spectral luminosity density from dust and stars as a function of wavelength is shown in Figure 5. The spectrally integrated luminosity density of *IRAS* galaxies is $0.53 \times 10^8\ L_\odot\ \mathrm{Mpc^{-3}}$, which, together with the stellar UV to near-IR local luminosity density of $1.3 \times 10^8\ L_\odot\ \mathrm{Mpc^{-3}}$, gives a total observed luminosity density of $\epsilon(\nu, 0) \approx (1.8 \pm 0.7) \times 10^8\ L_\odot\ \mathrm{Mpc^{-3}}$. We assumed here that the uncertainties in the local luminosity density are dominated by those in the stellar component. Table 2 compares the current luminosity density to that predicted by the various cosmic star formation scenarios discussed in § 4. The table shows that the PF95 infall model predicts a local luminosity density of $\sim 4 \times 10^8\ L_\odot\ \mathrm{Mpc^{-3}}$, significantly larger than the observed value. The model can, however, be modified to fit the observational constraint if, for example, a fraction of the star formation activity at some epoch results in the production of massive stars that release all of their radiative energy instantaneously back into space. All other star formation scenarios reproduce the local luminosity density within the uncertainty of the observations.

The observed $\epsilon_d(\nu, 0)/\epsilon(\nu, 0)$ ratio is 0.30, suggesting that locally, about 30% of the stellar light is processed by dust into thermal IR emission. The attenuated stellar spectral luminosity density, $\epsilon_s(\nu, 0)$, can be derived by propagating the spectral luminosity density of the sources, $\epsilon(\nu, 0)$, through a foreground screen characterized by a Galactic extinction law with a visual optical depth of $\tau_{abs}(V) \approx 0.27$.

6. ASTROPHYSICAL IMPLICATIONS

6.1. *Summary of EBL Detections and Observational Constraints*

Figure 8 depicts the current detection and observational constraints on the EBL at UV to far-IR wavelengths. The figure shows the DIRBE 140 and 240 μm detections plotted with 2 σ error bars (Paper I), the 100 μm lower limit estimated in § 3, and the FIRAS 125 to 5000 μm detection (Fixsen et al. 1998, plotted here only between 200 and 1000 μm). Figure 8 also shows the DIRBE 2 σ upper limits in the 1.25–100 μm wavelength region, where foreground emissions from interplanetary dust and the Galaxy were the main obstacles for the detection of any extragalactic signal.

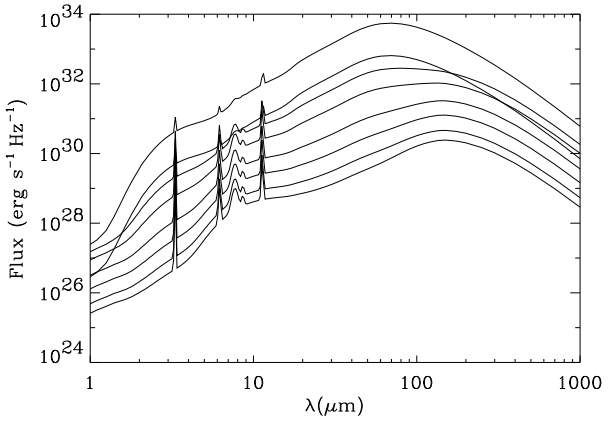

FIG. 7.—Spectral luminosity of representative *IRAS* galaxies listed in Table 3. The lowest curve represents that of normal galaxies ($L_{IR} < 3 \times 10^9\ L_\odot$), whereas the highest curve represents that of the most luminous *IRAS* galaxies ($L_{IR} > 10^{13}\ L_\odot$).

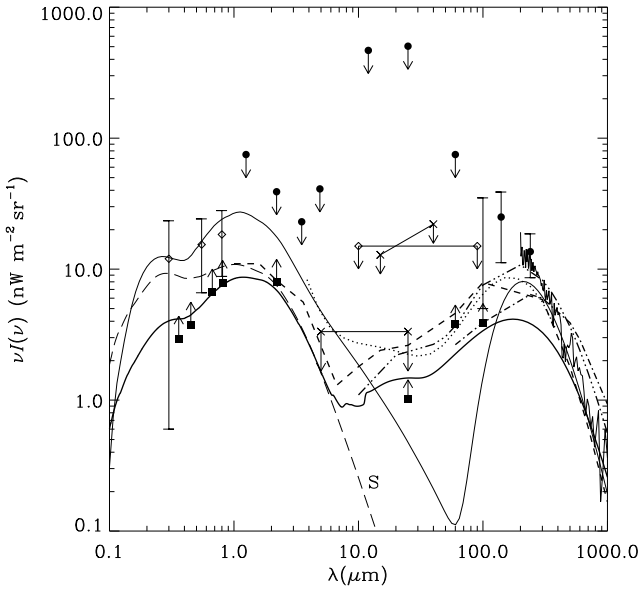

FIG. 8.—Model calculations of the EBL spectrum are compared with the *COBE* results. The DIRBE 2 σ upper limits at 1.25–60 μm and detections at 140 and 240 μm with ± 2 σ error bars are represented by solid circles (Paper I). The 100 μm intensity is represented by the 95% confidence limit of 5–34 nW m^{-2} sr^{-1}. The FIRAS 125–5000 μm detection (Fixsen et al. 1997) is shown by a light solid line; the UV-optical lower limits of Pozzetti et al. (1998) and the 2.2 μm lower limit (Gardner 1996) are represented by solid squares. The crosses represent the upper limits on the EBL derived from TeV observations of Mrk 501 (Stanev & Franceschini 1998) and Mrk 421 (Dwek & Slavin 1994), and the open diamonds represent the upper limits derived from the analysis of the fluctuations the DIRBE maps (KMO96). The heavy solid curve represents the EBL spectrum calculated from the UVO model in this paper. Other models presented in the figure are the backward evolution models of Malkan & Stecker (1998; *dotted line*) and of Beichman & Helou (1991; *dashed dotted line*), the forward evolution models of Franceschini et al. (1997, *dashed line*) and Guiderdoni et al. (1997, *dashed triple dotted line*), and the cosmic chemical evolution model of Fall, Charlot, & Pei (1996, *thin solid line*). The dashed line marked *S* represents the EBL spectrum calculated for a dust-free universe with the UVO cosmic star formation rate.

Upper limits on the intensity of the EBL can also be derived from a comparison of the spatial fluctuations in the DIRBE maps with those expected from spatial fluctuations of galaxy clusters (Kashlinsky et al. 1996b). In the 10–100 μm wavelength region, the fluctuation analysis suggests an upper limit of 10–15 nW m^{-2} sr^{-1} (Kashlinsky, Mather, & Odenwald 1996a; hereafter KMO96).

TeV γ-ray observations of active galaxies can, in principle, provide additional constraints on the intensity of the EBL at IR wavelengths (e.g., Stecker & De Jager 1993). TeV γ-rays interact primarily with 5–40 μm photons from the EBL by e^+e^- pair production. Any evidence for absorption in the spectra of the various TeV γ-ray sources could therefore be used to infer the energy density of the EBL in this wavelength region. In practice, these calculations require knowledge of the intrinsic γ-ray spectrum of the source, and the shape of the EBL in the $\sim$5–40 μm wavelength regime (Dwek & Slavin 1994). Currently, there is no evidence for any intergalactic absorption in the spectrum of the three TeV sources detected to date (Krennrich et al. 1997; Catanese et al. 1997). Claimed detections of, or upper limits on the EBL from TeV γ-ray observations should therefore be regarded as preliminary at present. Nevertheless, we show in Figure 7 the 15–40 μm upper limits derived from the γ-ray spectrum of Mrk 421 (Dwek & Slavin 1994), and the 5–25 μm upper limits derived from the observations of Mrk 501 (Stanev & Franceschini 1998). Although these limits are well below the direct observational limits of the DIRBE (Paper I), they are no stricter than those obtained by KMO96, and considering their uncertainty, provide soft constraints on currently popular models in this wavelength interval.

Figure 8 also shows the UV and optical lower limits derived from *HST* observations of the HDF (Pozzetti et al. 1998), the near-IR lower limits from galaxy counts (Gardner 1996), the 25, 60, and 100 μm lower limits from *IRAS* galaxy counts (Hacking & Soifer 1991; Gregorich et al. 1995), and the recent optical detections at 0.3, 0.55, and 0.8 μm by Bernstein (1997) and Bernstein et al. (1998).

6.2. *Comparison of Observations with Model Calculations*

Figure 8 compares the EBL detections and constraints with various model predictions in the 0.1 to 1000 μm wavelength regime. The thick solid line represents the spectrum of the EBL predicted by our hybrid forward-backward cosmic chemical evolution model described in § 5.1, using the UVO cosmic SFR (hereafter referred to as the UVO model). The discontinuities in the flux at 7.7, 8.6, and 11.3 μm result from the cumulative contribution of the respective PAH emission lines to the EBL. Also shown in the figure are the backward evolution models of Beichman & Helou (1991, BH) and Malkan & Stecker (1998, MS), the forward evolution model of Franceschini et al. (1997, FR) and Guiderdoni et al. (1997, hereafter GD), and the cosmic chemical evolution infall model of Fall et al. (1996, FCP). The curve labeled *S* represents a dust-free model, calculated with the UVO star formation rate in which galactic starlight is allowed to escape into space unimpeded by dust. The curve illustrates the obvious, namely that in order to have *any* significant far-IR emission, a fraction of the starlight has to be reprocessed by dust.

Postponing the discussion of the results of the UVO model for the moment, in a broad sense, all other models depicted in the figure, with the exception of the BH and FCP models, fall within 3 σ of the DIRBE 140 μm detection, and all models fall within 3 σ of the 240 μm detection. Most models are also consistent with the FIRAS detection of Fixsen et al. (1998), except for models GD and BH, which predict a somewhat higher flux at wavelengths $\gtrsim$500 μm. The various models differ most in their predicted 5–60 μm intensities. The FCP model falls especially short in this wavelength region, since (admittedly) the authors did not attempt to model the dust emission at these wavelengths.

Very obvious in the figure is the failure of the UV-optically determined star formation rate to produce the observed EBL at far-IR wavelengths. Observationally this should not be too surprising since the most intense star-forming regions frequently manifest themselves primarily through their infrared, rather than their UV or optical, emission, as recently illustrated by *ISO* observations of the Antennae galaxies (Mirabel et al. 1998). Furthermore, we have already shown that the total integrated EBL intensity predicted by the UVO cosmic SFR was very close to the detected EBL at 0.36–2.2 μm and 140–5000 μm, leaving no room for any EBL intensity in the $\sim$2–140 μm region of the spectrum. Since our template dust spectrum includes significant emission in this spectral wavelength region, the far-IR intensity predicted by the UVO model must fall significantly below the observations. The calculated far-IR intensity cannot be increased by simply increasing the fraction of starlight that is reradiated in the model as thermal IR emission. This will require an increase in the extinction, causing the UV-optical part of the EBL to fall below the lower limits of Pozzetti et al. (1998). It seems clear that the excess IR emission needed to account for the detected EBL requires a star formation activity that escaped detection at UV and optical wavelengths.

6.3. *Are There UV-Optically "Hidden" Galaxies or Star-forming Regions in the Universe?*

The existence of optically obscured star-forming regions is not only suggested by the discrepancy of the UVO model EBL spectrum and the observations. Figure 8 shows that *all* model predictions are 2 σ below the DIRBE EBL measurement at 140 μm, which is consistent with the somewhat noisier FIRAS determination at this wavelength. A population of optically hidden, dust-enshrouded galaxies or star-forming regions may therefore be needed to account for the observed infrared component of the EBL in all models.

We therefore considered various additional star formation histories. The cosmic SFRs predicted by the infall or closed box models of PF95 (labeled PFI and PFC, respectively, in Fig. 3) offer alternatives to the UVO model, since they a priori predict higher values for the integrated EBL intensity (see § 4 and Table 2). Since the integrated EBL of the PFI model is significantly larger than that predicted by the UVO model, it can produce the observed infrared EBL with less extinction than the UVO model, whereas the PFC model requires a somewhat larger extinction to reproduce the observations. We therefore calculated the EBL spectrum using the PFI and PFC star formation rates with $\tau_{abs}(V)$ values of 0.20 and 0.35, respectively. The results of these calculations are presented in Figure 9. For comparison, the figure also presents the results of the UVO model, as well as a schematic presentation of the range of $\nu I(\nu)$ values allowed by the various observational constraints and detections in the form of a shaded band. The detailed constraints were discussed earlier in § 6.1 and presented in

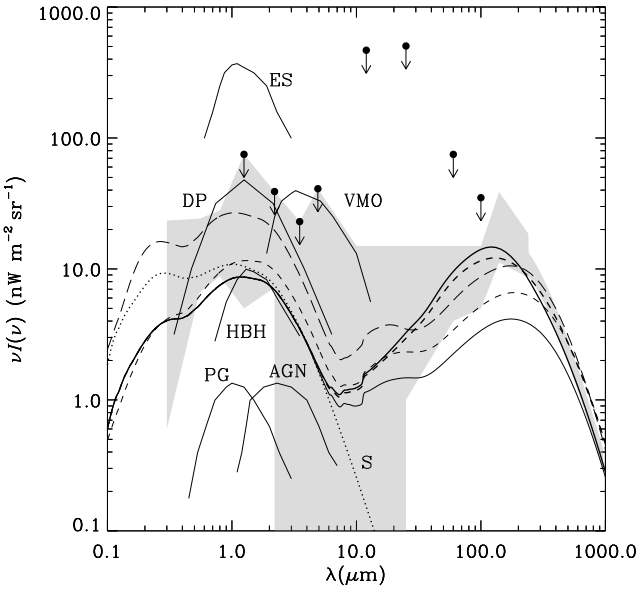

FIG. 9.—Observational constraints from Fig. 8 (represented here by a shaded area) are compared with the EBL calculated for several different cosmic star formation histories. The DIRBE and FIRAS detections are represented by the $\pm 2\ \sigma$ uncertainties in their values, and the DIRBE 2 σ upper limits are represented by solid circles. The 10–100 μm upper boundary of the shaded area represents the KMO96 upper limit. The thin solid line represents the EBL predicted by our model using the UVO cosmic SFR (see also Fig. 8). The long- and short-dashed curves represent the EBL predicted by our model using the PFI and PFC star formation rates, respectively. The two thick lines represent the EBL predicted if the UV-optically determined cosmic SFR is augmented by a "hidden" component representing the star formation activity taking place in dust-enshrouded galaxies or star-forming regions. The thick solid line represents the EBL if the excess luminosity density of these objects is distributed with redshift as the curve marked ED in Fig. 4, and the thick dashed line assumes an excess luminosity density that varies with redshift as the curve marked RR in Fig. 4. Also shown in the figure are the EBL spectra of various sources postulated by BCH86 and BCH91: exploding stars (ES), decaying particles (DP), very massive objects (VMO), halo black holes (HBH), primeval galaxies (PG), and AGNs, all calculated for $H_0 = 50$ km s^{-1} Mpc^{-1}. The dotted line marked *S* represents the EBL spectrum calculated for a dust-free universe with the UVO cosmic star formation rate.

Figure 8. For the purpose of the discussion, we chose to represent the upper limit in the 10–100 μm region by the value determined from the KMO96 fluctuation analysis, instead of the larger, but more definitive direct DIRBE limits (Paper I).

The results show that the PFC model gives an acceptable fit to the EBL at $\lambda \gtrsim 100$ μm. The discrepancies, the excess at $\lambda \gtrsim 400$ μm and the deficiency at ~ 140 μm, can be reduced by adopting a somewhat hotter spectrum for the emerging IR emission. The PFI model provides a better fit to the IR detections but overestimates the local UV to near-IR luminosity density (see Table 2). However, the local luminosity density predicted by this model can be lowered if a significant fraction of the star formation produces massive stars that recycle their energy instantaneously back to the ISM.

To explore the predictions of such a two-component star formation scenario in more detail, we constructed a cosmic SFR that consists of the following sum:

$$\psi(z) = \psi_{\rm UVO}(z) + C\psi_{\rm UVO}(z)\left[1 + \frac{\psi_{\rm UVO}(z)}{\psi_0}\right]^{20}, \quad (27)$$

where the first term represents the UVO cosmic SFR and the second term represents an additional star formation rate component that produces massive stars. The latter component may be responsible for the observed iron enrichment in the intracluster medium (Elbaz, Arnaud, & Vangioni-Flam 1995; Zepf & Silk 1996). By construction, the functional form of the second component is sharply peaked at the maximum of $\psi_{\rm UVO}(z)$, $\psi_0 = 1$ yr^{-1} Mpc^{-3}, and C is a normalization constant, adjusted to provide an improved fit to the detected IR background. Figure 3 depicts the behavior of this SFR (hereafter ED) as a function of redshift, for $C = 4.8 \times 10^{-3}$. To examine the possibility that the cosmic SFR was significantly higher at redshifts above ~ 1.5, as may be implied by the *ISO* observations of the HDF (RR97), we constructed an additional two-component cosmic SFR similar in form to the one given in equation (27). In this model (hereafter RR), the first component is equal to $\psi_{\rm UVO}(z)$ and the second component is equal to $1.9 \times 10^{-3}\ \psi_{\rm UVO}(z)[1 + \psi_{\rm UVO}(z)/\psi_0]^{20}$ at redshifts $\lesssim 1.5$ and constant at its peak value at higher redshifts. The behavior of this SFR is also depicted in Figure 3. We assume that stars formed by the second component are massive and release all their radiative output instantaneously into the ISM, where it is totally absorbed by dust. This is required because a Salpeter IMF overproduces the local K-band luminosity density by more than $\sim 50\%$. The contribution of the second components to the luminosity density at various redshifts is shown in Figure 4. The observed excess IR background emission, over that predicted by the various models shown in Figure 8, requires the rest frame spectra of these dusty, optically opaque galaxies or star-forming regions to peak shortward of ~ 100 μm. We therefore further assume that these opaque sources have a ULIRG spectrum, characterized by that of an H II region (Fig. 6). The EBL spectrum predicted by this two-component SFR is therefore equal to the sum of that predicted by the UVO model plus the cumulative redshifted IR emission arising from the second SFR component.

The resulting EBL spectra predicted by the two two-component models are shown in Figure 9. Both models provide a significantly improved fit to the IR background compared to *all* other model predictions and by construction produce the local luminosity density at IR and UV-optical wavelengths. The RR model predicts a somewhat larger IR background above ~ 200 μm than the ED model, since a larger fraction of its star formation rate takes place at higher redshifts. The ED model requires the luminosity density at $z \approx 1.5$ to be higher than that predicted by the UVO model by about $\sim 2 \times 10^9\ L_\odot$ Mpc^{-3} (Fig. 4). If these sources are identified with ULIRGs having $L \approx 10^{13}\ L_\odot$, then the required number density of such galaxies would be $\sim 10^{-4}$ Mpc^{-3}, about 10^4 times higher than that observed in the local universe. Current observations suggest only a mild evolution in the ULIRG population up to $z \lesssim 0.1$ (e.g., Ashby et al. 1996; see also Sanders & Mirabel 1996). Extrapolated to $z \approx 1$, this evolutionary trend yields an enhancement in the ULIRG number density by a factor of only ~ 100 over the local value. Alternatively, the excess emission could take place in dust-enshrouded starburst regions in a population of optically faint, but more numerous, galaxies that may have since dispersed their dust and evolved into the more familiar objects seen today.

Figure 9 also shows the contribution of several unobscured "exotic" sources to the EBL (BCH86, BCH91). As discussed in Paper I, the contribution of some sources to the EBL can already be ruled out from the DIRBE upper limits

in the 1.25 to 4.9 μm wavelength region. Complete obscuration of these sources by dust would move their spectra horizontally to longer wavelengths, with the location of the peak determined by the absorbing dust temperature. With some modification, these sources could contribute to the far-IR spectrum of the EBL. The possibility that some exotic and nonnuclear energy sources may contribute to the EBL and the fact that the ED and RR star formation histories produce similar IR background spectra shows that there is no unique way to account for the EBL spectrum. The current ambiguity in the magnitude and evolution of the cosmic star formation rate can only be resolved by future measurements of high-z systems at infrared wavelengths.

7. CONCLUSIONS

In this paper we examined some cosmological implications of the DIRBE and FIRAS detections of the EBL at wavelengths between 140 to 5000 μm. We first showed that the residual isotropic infrared background is not likely to arise from local sources in the solar system or in the Galaxy (§ 2). The DIRBE 140 and 240 μm and FIRAS 125–5000 μm residuals are therefore of extragalactic origin. Assuming that the 140 and 240 background radiation arises from dust emission, we used the measured intensities to derive a lower limit of 5 nW m^{-2} sr^{-1} for the extragalactic contribution at 100 μm.

The integrated EBL intensity detected by *COBE* in the 140–1000 μm wavelength region is $\sim$16 nW m^{-2} sr^{-1}. This intensity is consistent with the energy release expected from nuclear energy sources and constitutes about 20%–50% of the total energy released in the formation of He and metals throughout the history of the universe, the range reflecting various cosmic star formation histories considered in § 4. Galaxy number counts provide a lower limit of 12 nW m^{-2} sr^{-1} on the EBL intensity in the 0.36 to 2.2 μm wavelength interval. The explored regions of the EBL account therefore for a total intensity in excess of 28 nW m^{-2} sr^{-1}. Attributed only to nuclear sources, this intensity implies that more than $\sim$10% of the baryonic mass density implied by big bang nucleosynthesis analysis has been processed in stars to He and heavier elements.

We examined the constraints set by the total intensity of the EBL detected by the *COBE* on the cosmological star formation rate (SFR), in particular, on the recently published rate compiled by MPD98 from UV and optical (UVO) observations. The EBL intensity predicted by this cosmic SFR is about 30 nW m^{-2} sr^{-1}, comparable to the EBL intensity in the 0.36–2.2 and 140–5000 μm wavelength regions. This leaves no room for any expected EBL in the $\sim$2–140 μm wavelength interval. This suggests that the UVO cosmic SFR missed a significant fraction of the cosmic star formation activity that takes place in dust-enshrouded galaxies or star-forming regions.

We constructed a detailed model for calculating the spectrum of the EBL using a hybrid of forward, backward, and cosmic chemical evolution models. We calculated the EBL spectrum predicted for the UVO cosmic SFR and compared this spectrum, as well as those predicted by other selected models, to the observational constraints (Fig. 8). The IR background predicted by the UVO star formation rate falls considerably short of the *COBE* detections. We therefore examined various alternative cosmic star formation histories. In particular we constructed a two-component cosmic SFR consisting of the UVO star formation rate plus an additional component representing the star formation activity that might be going on in dust-enshrouded galaxies or star-forming regions. Two such models, characterized by different behavior of the excess star formation activity at high redshifts, were considered (see Figs. 3 and 4). The EBL spectra predicted by these two models are very similar and provide significantly better fits to the nominal *COBE* detections (Fig. 9). The excess stellar energy must be generated mainly by massive stars that may be the source of the observed metal enrichment of the intracluster medium.

Although there is currently no compelling need to invoke nonnuclear energy sources to explain the *COBE* data, their potential contribution to the observed EBL cannot be ruled out. However, the magnitude and spectral shape of any such proposed contribution must now be consistent with the *COBE* upper limits and detections. Their contribution, as well as the nucleosynthetic contribution to the EBL, cannot be unambiguously determined from the *COBE* data alone and must await the results of future observations that will resolve the sources of the EBL.

We acknowledge helpful discussions with Jim Felten, Jonathan Gardner, Alexander Kashlinsky, Richard Larson, Simon Lilly, Piero Madau, Bill Reach, Dave Sanders, and Vic Teplitz. We thank Alberto Franceschini, Bruno Guiderdoni, and Matt Malkan for communicating their model calculations and Piero Madau for providing his updated cosmic SFR. We thank Rebecca Bernstein for communicating her optical data prior to publication. We thank Steve Shore and the referee Adolf Witt for their enthusiastic response to the paper and for suggestions that led us to consider more detailed modeling of the EBL spectrum. The authors also gratefully acknowledge the contributions over many years of the many engineers, managers, scientists, analysts, and programmers engaged in the *COBE* investigation. The National Aeronautics and Space Administration/Goddard Space Flight Center (NASA/GSFC) was responsible for the design, development, and operation of the *COBE*. The GSFC was also responsible for the development of the analysis software and for the production of the mission data sets. Scientific guidance is provided by the *COBE* Science Working Group.

APPENDIX

DISRUPTIVE FORCES AND INTERACTION TIMESCALES FOR A HYPOTHETICAL SOLAR SYSTEM CLOUD

In the following we examine the lifetime of a hypothetical cloud of particles in the solar system, with properties constrained to produce an isotropic far-IR emission component comparable to the observed DIRBE residuals, against various disruptive

processes in the solar system and the ISM. A similar study was conducted by Stern (1990), who considered the physical interaction between the ISM and the Oort cloud. To set strict upper limits on the stability of this hypothetical cloud we will assume that it consists of refractory particles with a mass density $\rho = 3$ g cm^{-3}.

A1. PARTICLE CLOUD INTERACTION WITH THE INTERSTELLAR MEDIUM

Interactions with charged constituents of the ISM are clearly important if the particle cloud is located outside the heliosphere, the cavity carved out from the ISM by the solar wind. The radius of this cavity is determined by the distance at which the magnetic pressure of the solar wind equals that of the ISM and could be anywhere between 50 and 150 AU (Holtzer 1989). We will assume that interactions with the ISM can also take place within the heliosphere, since the *Ulysses* spacecraft has detected a flux of interstellar dust particles in the solar system (Grün et al. 1994) and neutral atoms can penetrate the heliosphere in a similar fashion.

The solar system moves at a velocity $v_\odot \approx 20$ km s^{-1} relative to the ISM gas (Spitzer 1978). This motion will take the solar system through various ISM phases characterized by different densities (n), temperatures (T), and filling factors (f): the hot ionized medium (HIM) characterized by (n_h, T_h, f_h) = (0.005 cm^{-3}, 10^6 K, 0.2–0.6), the warm neutral medium (WNM) characterized by (n_w, T_w, f_w) = (0.26 cm^{-3}, 8000 K, $\sim$0.3), and the cold neutral medium (CNM) characterized by (n_c, T_c, f_c) = (40 cm^{-3}, 50 K, $\sim$0.02). The average ISM density traversed by the solar system is therefore $n_0 \sim 1$ cm^{-3}.

Thermal sputtering will be most important when the solar system passes through the HIM. The sputtering lifetime of a refractory dust particle of radius a embedded in a gas of number density n and temperature $T \approx 10^6$ K is (Dwek, Foster, & Vancura 1996)

$$\tau_{\rm sput} \approx 5 \times 10^6 \, \frac{a(\mu{\rm m})}{n({\rm cm}^{-3})} \, {\rm yr} \, . \tag{A1}$$

When an HIM filling factor of 0.4 is adopted, the solar system has spent a total of $\sim 1.8 \times 10^9$ yr in the HIM. Any dust particles with radii $\lesssim 1.8$ μm would therefore have been eroded away by thermal sputtering during this time period.

Drag will become important when a particle has swept up the equivalent of its own mass. The drag time is therefore given by

$$\begin{aligned} \tau_{\rm drag} &= \frac{4\rho a}{3 n_0 \, v_\odot \, \mu m_{\rm H}} \\ &= 2.7 \times 10^{10} a({\rm cm}) \ {\rm yr}, \end{aligned} \tag{A2}$$

where we used $\rho \approx 3$ g cm^{-3} for the average density of a particle and $\mu \approx 1.4$ as the mean molecular weight (in atomic mass units) of the ISM gas. Dust particles with radii $\lesssim 0.16$ cm will therefore be lost from the cloud by collisional drag with the ISM on a timescale $\lesssim \tau_\odot$.

Kinetic sputtering is important when dust particles move at suprathermal speed through the ISM. The timescale for destruction by kinetic sputtering following a collision with ISM gas atoms with number density n_A and mass m_A is

$$\tau_{\rm kin} = \frac{4\rho a}{3 n_A \, v_\odot \, \mu_{\rm sp} \, m_{\rm H} \, Y(E)} \, , \tag{A3}$$

where $\mu_{\rm sp} \approx 20$ is the atomic mass of a sputtered particle and $Y(E)$ is the sputtering yield (defined as the number of ejected particles per incident projectile) at energy $E = \frac{1}{2} m_A v_\odot^2$. At velocities of 20 km s^{-1}, H, He, and C atoms will impinge on the cloud particles with kinetic energies of 2, 8, and 24 eV, respectively. Comparison of the drag and kinetic sputtering timescales gives

$$\frac{\tau_{\rm drag}}{\tau_{\rm kin}} = \frac{n_A \, \mu_{\rm sp} \, Y(E)}{n_{\rm H} \, \mu} \, . \tag{A4}$$

Sputtering thresholds range from $\sim$5 to 8 eV for the most common refractory material, so that only sputtering by He or C atoms will be important, giving $n_A \, \mu_{\rm sp} / n_{\rm H} \, \mu \sim 1$. Furthermore, close to the sputtering threshold, $Y(E) \ll 1$. Consequently, cloud disruption by kinetic sputtering can be neglected compared to its erosion by collisional drag.

Evaporative collisions with interstellar grains are not an important destruction process for the cloud particles. Laboratory experiments on collisions between refractory rocks (O'Keefe & Ahrens 1982) show that complete vaporization occurred only when the kinetic energy per projectile atom exceeded the material binding energy (typically 5–8 eV) by factors $\gtrsim 5$. These correspond to impact velocities $\gtrsim 30$ km s^{-1}, well above the relative velocity of the solar system particle cloud with the ISM. However, the slow and continuous erosion of the cloud particles by cratering collisions proceeds at much lower impact velocities and can be an important destruction process. Following Borkowski & Dwek (1995) we write the erosion rate due to cratering collisions as

$$\left(\frac{dm}{dt} \right)_{\rm cr} = \pi a^2 n_d(m_d) v_\odot \, m_A \, Y_{\rm cr}(E) \, , \tag{A5}$$

where $n_d(m_d)$ is the number density of interstellar dust grains (i.e., projectiles) of mass m_d, m_A is the mass of an individual atom in the target material, and $Y_{\rm cr} = m_d \, v_\odot^2 / 2E_{\rm cr}$ is a dimensionless cratering yield, where $E_{\rm cr}$ is the specific energy for the ejection of one atom in a cratering event, typically $\sim$1 eV. The product $m_A Y_{\rm cr}$ is thus equal to the total mass excavated in the cratering

event, and the validity of the expression requires it to be significantly less than m, the mass of the target grain. The timescale for particle erosion by cratering collisions is simply given by $m/\dot{m}_{\rm cr}$:

$$\tau_{\rm cr} = \frac{4\rho a}{3n_0 v_\odot Z_d \mu m_{\rm H}} \left(\frac{m_A v_\odot^2}{2E_{\rm cr}}\right)^{-1} = 6.8 \times 10^{10} a({\rm cm})\ {\rm yr}\ , \tag{A6}$$

where we used the relation: $n_d(m_d)m_d = Z_d n_0 \mu m_{\rm H}$, with $Z_d = 0.01$ as the dust-to-gas mass ratio in the ISM, $m_A = 20\ m_{\rm H}$, and $E_{\rm cr} = 1$ eV. Equation (9) is valid only for particles with $m \gtrsim 40\ m_d$ or $a \gtrsim 4\ \mu$m, where we adopted a grain radius of $\sim 1\ \mu$m for the largest interstellar dust particles. Hence cloud particles with sizes less than ~ 0.07 cm will be eroded by cratering collisions with interstellar dust particles.

A2. FORCES WITHIN THE SOLAR SYSTEM

Particles within the heliosphere will also be subjected to local forces caused by the Sun's gravity, its radiation, and the solar wind. Depending on the optical properties, mass, and heliocentric distance of the particles, they can spiral into the Sun, be blown out of the solar system, or remain unaffected by the combined effect of these forces. The absorption and reradiation of sunlight by the orbiting particles gives rise to a Poynting-Robertson (P-R) drag. The decay time for heliocentric orbits of radius d as a result of the P-R drag is given by Burns, Lamy, & Soter (1979, hereafter BLS79)

$$\tau_{\rm P\text{-}R} = \frac{mc^2}{4F_\odot(d)\pi a^2 Q_{\rm pr}} = 7 \times 10^2\ \frac{\rho a(\mu{\rm m}) d^2({\rm AU})}{Q_{\rm pr}}\ {\rm yr}\ , \tag{A7}$$

where $F_\odot(d)$ is the solar bolometric flux at distance d and $Q_{\rm pr}$ is the solar spectrum averaged radiation pressure efficiency factor of the particle (see below). A lower limit on the radius of the particles that will survive the P-R effect can be obtained by adopting a large heliopause radius of 150 AU. At this distance the critical radius above which particles will maintain a stable orbit over the lifetime of the solar system is given by $a_{\rm crit}(\mu{\rm m}) = 95 Q_{\rm pr}$.

Radiation pressure can also expel particles from the solar system, if it overcomes the Sun's gravitational attraction. Following BLS79, we define the parameter β as the ratio between the two forces:

$$\beta \equiv \frac{F_{\rm rad}}{F_{\rm grav}} = 0.57\ \frac{Q_{\rm pr}}{\rho a(\mu{\rm m})}\ . \tag{A8}$$

Particles with $\beta \geq \frac{1}{2}$ can escape the solar system (BLS79). Grains with radii of $a_{\rm exp}(\mu{\rm m}) \leq 0.09 Q_{\rm pr}$ can therefore be expelled from the solar system by radiation pressure. These radii are smaller than $a_{\rm crit}$, so particles that are stable against the P-R effect are also stable against expulsion from the solar system by radiation pressure.

The radiation pressure efficiency factor of the particle is given by $Q_{\rm pr} = Q_{\rm ext}(1 - \langle\cos\theta\rangle A)$, where $Q_{\rm ext}$ is the extinction efficiency of the particle, A its albedo, and $\langle\cos\theta\rangle$ is a measure of its forward scattering efficiency. For a strongly forward scattering particle $\langle\cos\theta\rangle \approx 1$, whereas for an isotropically scattering particle $\langle\cos\theta\rangle \approx 0$. Particles with radii significantly greater than the wavelength of the incident radiation are strong forward scatterers, and applying geometrical optics one gets a value of $Q_{\rm pr} \approx 0.5$, and $Q_{\rm ext} \approx 1$.

A3. GRAVITATIONAL PERTURBATIONS FROM PASSING STARS

Any cloud of particles cannot survive beyond the tidal radius R_T, at which the Galactic tidal forces on a particle are equal to the Sun's gravitational force. The tidal radius is given by Tremaine (1993)

$$R_T({\rm AU}) = 1.7 \times 10^5 \left(\frac{\rho_{\rm gal}}{0.15\ M_\odot\ {\rm pc}^{-3}}\right)^{-1/3} \tag{A9}$$

where $\rho_{\rm gal}$ is the local Galactic mass density. Outside this radius, cloud particles can be ejected from the solar system by gravitational perturbations from passing stars and other material. The half-life for this process is given by Weinberg, Shapiro, & Wasserman (1987) and Tremaine (1993)

$$\tau_{\rm gal} = 10^{14} d^{-1}({\rm AU}) \left(\frac{\rho_{\rm gal}}{0.15\ M_\odot\ {\rm pc}^{-3}}\right)^{-1}\ {\rm yr}\ . \tag{A10}$$

Cloud particles located at distances above 2×10^4 AU will therefore be stripped out of the solar system.

REFERENCES

Arendt, R. G., et al. 1998, ApJ, 508, 74 (Paper III)
Ashby, M. L. N., Hacking, P. B., Houck, J. R., Soifer, B. T., & Weisstein, E. W. 1996, ApJ, 456, 428
Aumann, H. H. 1988, AJ, 96, 1415
Aumann, H. H., & Good, J. C. 1990, ApJ, 350, 408
Beichman, C. A., & Helou, G. 1991, ApJ, 370, L1 (BH)
Bernstein, R. A. 1997, Ph.D. thesis, California Institute of Technology
Bernstein, R. A., Freedman, W. L., & Madore, B. F. 1998, in preparation
Boggess, N. W., et al. 1992, ApJ, 397, 420
Bond, J. R., Carr, B. J., & Hogan, C. J. 1986, ApJ, 306, 428 (BCH86)
———. 1991, ApJ, 367, 420 (BCH91)
Borkowski, K. J., & Dwek, E. 1995, ApJ, 454, 254
Bressan, A., Fagotto, F. D., Bertelli, G., & Chiosi, C. 1993, A&AS, 100, 647
Burns, J. A., Lamy, P. L., & Soter, S. 1979, Icarus, 40, 1 (BLS79)

Carr, B. J. 1992, in The Infrared and Submillimeter Sky after *COBE*, ed. M. Signore & C. Drupaz (Dordrecht: Kluwer), 213
Catanese, M., et al. 1997, ApJ, 487, L143
Charlot, S., Worthey, G., & Bressan, A. 1996, ApJ, 457, 625
Draine, B. T., & Lee, H. M. 1984, ApJ, 285, 89
Dwek, E. 1997, ApJ, 484, 779
———. 1998, ApJ, 501, 643
Dwek, E., ed. 1996, in AIP Conf. Proc. 348, Unveiling the Cosmic Infrared Background (New York: AIP)
Dwek, E., Foster, S. M., & Vancura, O. 1996, ApJ, 457, 244
Dwek, E., & Slavin, J. 1994, ApJ, 436, 696
Dwek, E., & Városi, F. 1996, in AIP Conf. Proc. 348, Unveiling the Cosmic Infrared Background, ed. E. Dwek (New York: AIP), 237
Dwek, E., et al. 1997, ApJ, 475, 565
Elbaz, D., Arnaud, M., & Vangioni-Flam, E. 1995, A&A, 303, 345
Ellis, R. S., Colless, M., Broadhurst, T., Heyl, J., & Glazebrook, K. 1996, MNRAS, 280, 235
Fall, S. M., Charlot, S., & Pei, Y. C. 1996, ApJ, 464, L43 (FCP)
Ferrara, A., Ferrini, F., Franco, J., & Barsella, B. 1991, ApJ, 381, 137
Fixsen, D. J., Dwek, E., Mather, J. C., Bennett, C. L., & Shafer, R. A. 1998, ApJ, 508, 123 (Paper V)
Fixsen, D. J., et al. 1997, ApJ, 490, 482
Franceschini, A., Granato, G., Mazzei, P., Danese, L., & De Zotti, G. 1996, in AIP Conf. Proc. 348, Unveiling the Cosmic Infrared Background, ed. E. Dwek (New York: AIP), 159
Franceschini, A., et al. 1997, preprint (astro-ph/9707080) (FR)
Gardner, I. P. 1996, in AIP Conf. Proc. 348, Unveiling the Cosmic Infrared Background, ed. E. Dwek (New York: AIP), 127
Gardner, J. P., Sharples, R. M., Frenk, C. S., & Carrasco, B. E. 1997, ApJ, 480, L99
Granato, G. L., Franceschini, A., & Danese, L. 1996, in AIP Conf. Proc. 348, Unveiling the Cosmic Infrared Background, ed. E. Dwek (New York: AIP), 226
Gregorich, D. T., Neugebauer, G., Soifer, B. T., Gunn, J. E., & Herter, T. L. 1995, AJ, 110, 259
Grün, E., et al. 1994, A&A, 286, 915
Guiderdoni, B., Bouchet, F. R., Puget, J.-L., Lagache, G., & Hivon, E. 1997, Nature, 390, 257 (GD)
Hacking, P. B., & Soifer, B. T. 1991, ApJ, 367, L49
Harwitt, M. 1970, Nuovo Cimento, 2, 253
Hauser, M. G., et al. 1998, ApJ, 508, 25 (Paper I)
Holtzer, T. E. 1989, ARA&A, 27, 199
Kashlinsky, A., Mather, J. C., & Odenwald, S. 1996a, ApJ, 473, L9 (KMO96)
Kashlinsky, A., Mather, J. C., Odenwald, S., & Hauser, M. G. 1996b, ApJ, 470, 681
Kelsall, T. J., et al. 1998, ApJ, 508, 44 (Paper II)
Klaas, U., Haas, M., Heinrichsen, I., & Schulz, B. 1997, A&A, 325, L21
Kolb, E. W., & Turner, M. S. 1990, The Early Universe (New York: Addison-Wesley)
Krennrich, F., et al. 1997, ApJ, 481, 758
Larson, R. B., & Tinsley, B. M. 1978, ApJ, 219, 46
Leinert, C. 1996, in AIP Conf. Proc. 348, Unveiling the Cosmic Infrared Background, ed. E. Dwek (New York: AIP), 53
Lilly, S. J., Le Fèvre, O., Hammer, F., & Crampton, D. 1996, ApJ, 460, L1
Lonsdale, C. 1995, in Extragalactic Background Radiation, ed. D. Calzetti, M. Livio, & P. Madao (Cambridge: Cambridge Univ. Press), 145
———. 1996, in AIP Conf. Proc. 348, Unveiling the Cosmic Infrared Background, ed. E. Dwek (New York: AIP), 147
Madau, P., Ferguson, H. C., Dickinson, M. E., Giavalisco, M., Steidel, C. C., & Fruchter, A. 1996, MNRAS, 283, 1388
Madau, P., Pozzetti, L., & Dickinson, M. 1998, ApJ, 498, 106 (MPD98)
Malkan, M. A., & Stecker, F. W. 1998, ApJ, 496, 13
Mirabel, I. F., et al. 1998, A&A, 333, L1
Negroponte, J. 1986, MNRAS, 222, 19
O'Keefe, J. D., & Ahrens, T. J. 1982, J. Geophys. Res., 87, 6668
Partridge, R. B., & Peebles, P. J. E. 1967, ApJ, 148, 377
Peebles, P. J. E. 1995, in Extragalactic Background Radiation, ed. D. Calzetti, M. Livio, & P. Madau (New York: Cambridge Univ. Press), 1
Pei, Y. C., & Fall, S. M. 1995, ApJ, 454, 69 (PF95)
Pettini, M., Smith, L. J., King, D. L., & Hunstead, R. W. 1997, ApJ, 486, 665
Pozzetti, L., Madau, P., Zamorani, G., Ferguson, H. C., & Bruzual, G. A. 1998, MNRAS, 298, 1133
Puget, J.-L., Abergel, A., Bernard, J.-P., Boulangerm, F., Burton, W. B., Désert, F.-X., & Hartmann, D. 1996, A&A, 308, L5
Rocca-Volmerange, B., & Fioc, M. 1996, in AIP Conf. Proc. 348, Unveiling the Cosmic Infrared Background, ed. E. Dwek (New York: AIP), 132
Rowan-Robinson, M., et al. 1997, MNRAS, 289, 490 (RR97)
Sanders, D. B., & Mirabel, I. F. 1996, ARA&A, 34, 749
Schlegel, D. J., Finkbeiner, D. P., & Davis, M. 1998, ApJ, 500, 525
Schmitt, H. R., Kinney, A. L., Calzetti, D., & Storchi Bergmann, T. S. 1997, AJ, 114, 592
Shafer, R. A., et al. 1998, ApJ, submitted
Shore, S. N., & Ferrini, F. 1995, Fundam. Cosmic Phys., 16, 1
Sodroski, T. J., Odegard, N., Arendt, R. A., Dwek, E., Weiland, J. P., Hauser, M. G., & Kelsall, T. 1997, ApJ, 480, 173
Soifer, B. T., & Neugebauer, G. 1991, AJ, 101, 354
Soifer, B. T., Sanders, D. B., Madore, B. F., Neugebauer, G., Lonsdale, C. J., Persson, S. E., & Rice, W. L. 1987, ApJ, 320, 238
Spitzer, L., Jr. 1978, Physical Processes in the Interstellar Medium (New York: Wiley)
Stanev, T., & Franceschini, A. 1998, ApJ, 494, L159
Stecker, F. W., & De Jager, O. C. 1993, ApJ, 415, L71
Steigman, G., Hata, N., & Felten, J. E. 1998, ApJ, in press (astro-ph/9708016)
Stern, A. 1990, Icarus, 84, 447
Teplitz, V. L., Rosenbaum, D. C., Scalise, R. J., Stern, S. A., & Anderson, J. D. 1998, The Problem of Mass, ed. B. Kursonoglu (New York: Plenum)
Tinsley, B. M. 1980, Fundam. Cosmic Phys., 5, 287
Tremaine, S. 1993, in ASP Conf. Ser. 36, Planets around Pulsars, ed. J. A. Phillips, J. E. Thorsett, & S. R. Kulkarni (San Francisco: ASP), 335
Wall, W. F., et al. 1996, ApJ, 456, 566
Weinberg, M. D., Shapiro, S. L., & Wasserman, I. 1987, ApJ, 312, 367
Witt, A. N., & Gordon, K. D. 1996, ApJ, 463, 681
Wright, E. L., et al. 1991, ApJ, 381, 200
Zaritsky, D. 1994, AJ, 108, 1619
Zepf, S. E., & Silk, J. 1996, ApJ, 466, 114